energies

MDPI

Article

A Low-Carbon Control Strategy for a Wind–Hydrogen–Ammonia Coupled Thermal Power System

Guitao Wang [1,2], Jifei Wang [1,2,*], Kai Qi [3], Suyao Liu [4] and Xinru Liu [1,2]

[1] College of Energy and Power Engineering, Inner Mongolia University of Technology, Hohhot 010080, China; 15313061186@163.com (G.W.); liuxinru1001@163.com (X.L.)
[2] Key Laboratory of Wind and Solar Energy Utilization Technology (Inner Mongolia University of Technology), Ministry of Education, Hohhot 010080, China
[3] Inner Mongolia Three Gorges Mengneng Energy Co., Ltd., Ordos 014300, China; qi_kai1@ctg.com.cn
[4] China Resources New Energy Investment Co., Ltd., Inner Mongolia Branch, Hohhot 010010, China; 1060863684lsy@gmail.com
* Correspondence: jifeiwang@imut.edu.cn; Tel.: +86-150-2914-1680

Abstract

As renewable energy integration increases, improving wind energy utilization and reducing carbon emissions from thermal power units have become key challenges for low-carbon power system operation. This study proposes a low-carbon control strategy for a wind–hydrogen–ammonia coupled thermal power system. First, a multi-energy-flow coupling model integrating wind-powered electrolytic hydrogen production, hydrogen storage, ammonia synthesis, and coal–ammonia co-firing is established. On this basis, a multi-objective interval-based energy management system (EMS) considering the temporal causality of hydrogen utilization is developed. The EMS explicitly distinguishes hydrogen stored at the end of the previous dispatch interval from hydrogen newly produced in the current interval. Hydrogen produced during the current dispatch interval cannot be directly used for ammonia synthesis within the same interval and is used only to update the end-of-interval hydrogen storage state. This treatment maintains temporal consistency among hydrogen production, storage, and utilization. Particle swarm optimization (PSO) is then employed to coordinate thermal power output and the ammonia co-firing ratio to reduce system operational CO_2 emissions and grid electricity purchases while smoothing thermal power output. The proposed strategy is evaluated through nine typical-day simulations, parameter sensitivity analyses, algorithm comparisons, and a year-round continuous simulation. Under the typical-day scenarios, the maximum system CO_2 emission reduction rate reaches 29.70%. PSO achieves system operational CO_2 emissions comparable to or lower than those obtained with the genetic algorithm (GA) and performs better overall than the single-step baseline method. In the year-round continuous simulation, system operational CO_2 emissions decrease from 998.968 kt for the pure-coal baseline under the same thermal power output trajectory to 961.255 kt, corresponding to an annual reduction rate of 3.78%. The annual average ammonia co-firing ratio is 7.21%. The results show that the proposed low-carbon control strategy can coordinate wind energy utilization, hydrogen–ammonia conversion, and low-carbon operation of thermal power units while satisfying multi-energy-flow operating constraints and the temporal causality of hydrogen utilization. This study provides a system-level control and dispatch approach for wind–hydrogen–ammonia coupled thermal power systems.

Keywords: wind power utilization; hydrogen storage; ammonia co-firing; multi-energy coupling; energy management strategy; particle swarm optimization

Check for updates

Academic Editor: Georg Frey

Received: 10 September 2026
Revised: 18 October 2026
Accepted: 29 October 2026
Published: 3 November 2026

Copyright: © 2026 by the authors. Licensee MDPI, Basel, Switzerland. This article is an open access article distributed under the terms and conditions of the Creative Commons Attribution (CC BY) license.

1. Introduction

Driven by carbon peaking and carbon neutrality goals and the accelerated development of new power systems, the power sector faces two major challenges: high renewable energy penetration and the low-carbon transition of thermal power units. Wind power is characterized by significant randomness and variability, and its large-scale integration increases the challenges of power balancing and flexible regulation in power systems. Meanwhile, thermal power units continue to provide essential support and regulation capabilities for power systems, while fuel combustion-related CO_2 emissions remain a major source of emissions in the power sector [1,2].

Integrated energy systems (IESs) enable the conversion, storage, and complementary utilization of multiple energy carriers, providing an effective pathway for renewable energy utilization and low-carbon system operation at the system level [3–5]. Existing studies have developed various energy hub models and coordinated optimization frameworks considering electricity, heat, gas, energy storage, and demand response [6–8]. Rolling optimization approaches, multi-timescale dispatch, and power-to-hydrogen technologies have been applied to enhance system flexibility under fluctuating renewable energy conditions [9–11]. With advances in hydrogen and ammonia technologies, energy coupling in power systems has gradually extended from conventional electricity–gas–heat systems to emerging electricity–hydrogen–ammonia chains. Hydrogen provides a means of converting renewable electricity into a storable energy carrier, while ammonia offers advantages in storage and transportation and can serve as both a hydrogen carrier and a fuel. Integrating renewable-based hydrogen production, hydrogen storage, ammonia synthesis, and fuel utilization creates opportunities for the inter-temporal utilization of variable renewable energy [12,13]. The carbon-reduction benefits of ammonia depend on its production pathway and utilization mode, highlighting the importance of well-defined emission accounting boundaries [14,15].

For thermal power units that continue to provide system regulation capabilities, partial coal substitution with ammonia offers a potential pathway for reducing direct CO_2 emissions from combustion. In recent years, research on coal–ammonia co-firing has progressed from fundamental combustion investigations to demonstrations in industrial-scale power units. In 2024, JERA and IHI conducted a demonstration of 20% ammonia substitution based on heat input in a 1GW-class coal-fired unit at Hekinan Thermal Power Station. The unit achieved operating performance comparable to pure-coal operation, while NO_x emissions remained at levels comparable to those under pure-coal operation [16]. Lin et al. further conducted industrial tests on a 300 MW coal-fired boiler under different load conditions and ammonia co-firing ratios, demonstrating the feasibility of coal–ammonia co-firing with ammonia heat input ratios of 10–20% [17]. These studies provide an important foundation for the engineering application of coal–ammonia co-firing. Nevertheless, unit-level combustion feasibility does not necessarily guarantee coordinated operation among wind-powered hydrogen production by electrolysis, hydrogen storage, ammonia synthesis, and ammonia co-firing in thermal power units. Under continuously fluctuating wind power conditions, the ammonia co-firing ratio needs to be coordinated with the hydrogen storage level through a system-level energy management strategy.

Considerable attention has been devoted to the scheduling and planning of hydrogen–ammonia coupled energy systems. Yuan et al. developed a bi-level optimal scheduling model for a wind–photovoltaic–thermal integrated energy system incorporating ammonia-based energy storage [18]. Liang et al. investigated coordinated low-carbon dispatch involving hydrogen storage, ammonia synthesis, carbon capture, and thermal power units [19]. Related studies have further explored coal–ammonia co-firing characteristics [20], the planning of hydrogen–ammonia co-firing systems [21], and coordinated ammonia syn-

thesis from multiple hydrogen sources [22]. Zhou et al. investigated the dynamically feasible operating range of a wind–photovoltaic hydrogen-to-ammonia system based on a multi-period dispatchable region perspective [23]. Recent studies have also incorporated wind power uncertainty, hydrogen storage, and green ammonia production into unified robust scheduling frameworks [24]. These studies indicate that hydrogen–ammonia system research is evolving from static energy balancing toward multi-period and dynamic operation modeling.

Compared with the above studies [18–24], the present study focuses specifically on the temporal availability of hydrogen in the dispatch-level operation of a wind–hydrogen–ammonia coupled thermal power system. In particular, the model explicitly distinguishes hydrogen stored at the end of the previous dispatch interval from hydrogen newly produced during the current dispatch interval. This inter-interval hydrogen-availability relationship is incorporated into an interval-based EMS to coordinate thermal power output and the ammonia co-firing ratio under hydrogen availability requirements and the dynamic operating constraints of thermal power units.

For the integrated process involving wind-powered hydrogen production by electrolysis, hydrogen storage, ammonia synthesis, and thermal power co-firing considered in this study, the available hydrogen in each dispatch interval needs to be clearly defined. In some system-level scheduling models, hydrogen produced within the current interval is directly allocated to ammonia synthesis. For example, the green ammonia scheduling model developed by Cheng and Ji considers two hydrogen utilization pathways: direct supply to ammonia synthesis and charging into hydrogen storage systems. Under this framework, hydrogen produced in the current interval can participate in ammonia synthesis during the same interval [25]. This formulation is suitable for systems with direct coupling between hydrogen production and ammonia synthesis. In contrast, the system considered in this study includes an intermediate hydrogen storage stage and follows a hydrogen production-storage-subsequent utilization sequence. Treating hydrogen production and consumption as occurring within the same interval may overestimate the hydrogen available for current operation and consequently affect the feasible ammonia co-firing ratio. To preserve the actual operating sequence, hydrogen stored at the end of the previous dispatch interval should be distinguished from hydrogen newly produced in the current interval. This distinction defines the hydrogen availability boundary across consecutive dispatch intervals. The ammonia co-firing ratio should therefore be coordinated with hydrogen availability, thermal power output, and the system state inherited from the previous dispatch interval. Incorporating these inter-interval relationships into the dispatch-interval-based EMS decision-making process forms the central scheduling problem addressed in this study.

To address these issues, this study proposes a low-carbon control strategy for a wind–hydrogen–ammonia coupled thermal power system, in which the temporal causality of hydrogen utilization is explicitly considered in the dispatch-interval-based EMS. The main contributions are summarized as follows:

(1) At the system-modeling level, a multi-energy-flow coupling model integrating wind-powered hydrogen production by electrolysis, hydrogen storage, ammonia synthesis, and coal–ammonia co-firing is developed. The temporal causality of hydrogen utilization is explicitly represented by distinguishing hydrogen stored at the end of the previous dispatch interval from newly produced hydrogen in the current dispatch interval. Hydrogen produced during the current dispatch interval is used only to update the end-of-interval hydrogen storage state and becomes available for ammonia synthesis only in subsequent dispatch intervals. This treatment maintains temporal consistency among hydrogen production, storage, and utilization.

(2) At the energy-management level, a multi-objective dispatch-interval-based EMS optimization framework is developed with thermal power output and the ammonia co-firing ratio as the primary decision variables. At each 0.5 h dispatch interval, PSO determines the operating point for the current interval based on the current wind–load conditions and the system states inherited from the previous dispatch interval. The EMS considers system operational CO_2 emissions, grid electricity purchases, thermal power output smoothing, the dynamic operating constraints of thermal power units, ammonia co-firing ratio adjustment constraints, hydrogen availability, and the temporal causality of hydrogen utilization. Its coordinated scheduling performance is evaluated through nine typical-day scenarios, parameter sensitivity analyses, algorithm comparisons, and year-round continuous simulation.

The remainder of this paper is organized as follows. Section 2 presents the energy-flow relationships, key models, and dynamic operating constraints of the wind–hydrogen–ammonia coupled thermal power system. Section 3 introduces the case-study data, system parameters, and simulation settings. Section 4 discusses the results under typical operating conditions, parameter sensitivity analyses, algorithm comparisons, and year-round continuous operation. Section 5 presents the main conclusions.

2. Modeling and Energy Management Strategy for the Wind–Hydrogen–Ammonia Coupled Thermal Power System

2.1. EMS Structure and Energy-Flow Relationships

The wind–hydrogen–ammonia coupled thermal power system developed in this study consists of a wind power system, an electrolytic hydrogen production system, a hydrogen storage system, an ammonia synthesis system, a coal–ammonia co-firing thermal power unit, an electrical load, and the grid. The overall system configuration is illustrated in Figure 1. Wind power serves as the primary renewable energy input, contributing to system power balancing and enabling inter-temporal energy transfer through hydrogen production by electrolysis and hydrogen storage. The stored hydrogen is subsequently used for ammonia synthesis, and the resulting ammonia is utilized as a low-carbon fuel for coal–ammonia co-firing in the thermal power unit, thereby reducing coal consumption and associated CO_2 emissions [26,27].

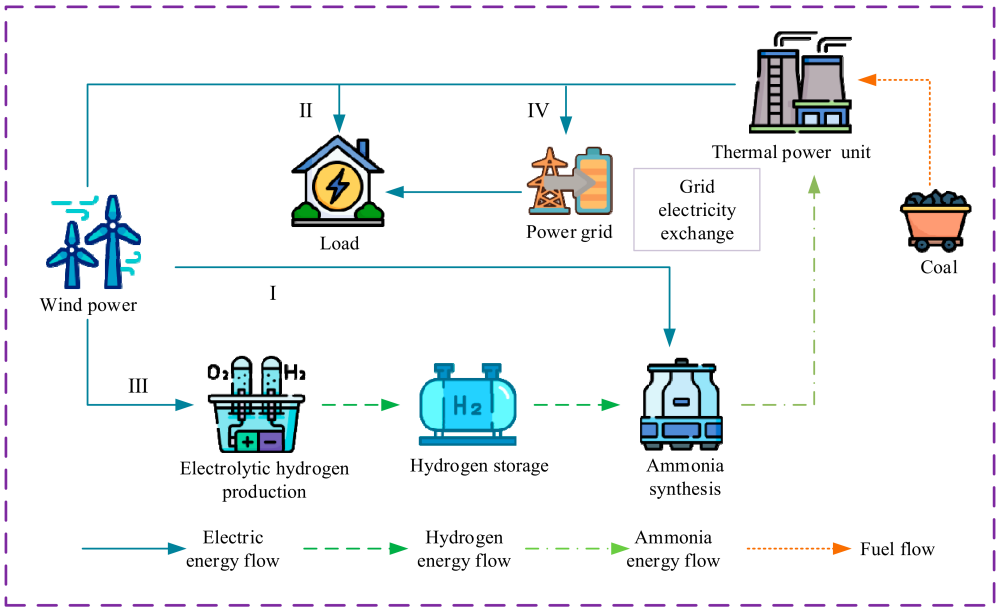


Figure 1. Structure of the wind–hydrogen–ammonia coupled thermal power system.

A dispatch interval of 0.5 h is adopted, and t denotes the current dispatch interval. Electrical energy is expressed in MWh/interval. The hydrogen storage state is represented by an energy-based variable expressed in MWh, which is used for dispatch-level hydrogen availability accounting.

During each dispatch interval, the EMS coordinates wind energy allocation among different subsystems according to a predefined sequence. Wind energy is first allocated to satisfy the electricity demand of ammonia synthesis, and then to supply the electrical load. Any remaining wind energy is directed to electrolytic hydrogen production. Thermal power output and grid electricity exchange jointly maintain the system power balance.

The energy balance equation is formulated as follows:

$$E_{\text{wind}}(t) + E_{\text{th}}(t) + E_{\text{grid}}(t) = E_{\text{load}}(t) + E_{\text{wind,H}_2}(t) + E_{\text{wind,NH}_3}(t) \quad (1)$$

where $E_{\text{wind}}(t)$ denotes the wind energy during dispatch interval t; $E_{\text{th}}(t)$ denotes the electrical energy output of the thermal power unit during dispatch interval t; $E_{\text{grid}}(t)$ denotes the grid electricity exchange; $E_{\text{load}}(t)$ denotes the electrical energy demand of the load; $E_{\text{wind,H}_2}(t)$ denotes the wind energy consumed for electrolytic hydrogen production; and $E_{\text{wind,NH}_3}(t)$ denotes the wind energy consumed for ammonia synthesis. A positive $E_{\text{grid}}(t)$ indicates electricity purchased from the grid, whereas a negative value indicates electricity sold to the grid.

From an energy-flow perspective, the system consists of three coupled energy pathways: electrical energy flow, hydrogen energy flow, and fuel flow. Wind energy and thermal power output jointly maintain the system power balance. Surplus wind energy is converted into hydrogen through the electrolyzer and stored in the hydrogen storage system. Hydrogen stored at the end of the previous dispatch interval is utilized for ammonia synthesis in the current interval. The synthesized ammonia partially substitutes coal as a fuel in thermal power units. These coupled multi-energy flows provide the physical basis for the subsequent interval-by-interval EMS optimization.

2.2. Coal Consumption, Coal–Ammonia Co-Firing, and CO_2 Emission Models for Thermal Power Units

(1) Ammonia co-firing model

Thermal power units provide essential power support for the system and remain a major source of direct CO_2 emissions during operation. To ensure consistency between fuel substitution and CO_2 emission accounting, pure-coal baseline consumption, coal substitution through coal–ammonia co-firing, and CO_2 emissions are modeled within a unified framework.

According to the coal consumption characteristics of thermal power units [28], the baseline coal consumption corresponding to the current thermal power output $E_{\text{th}}(t)$ under pure-coal operation is expressed as:

$$M_{\text{coal,base}}(t) = a_{\text{coal}} E_{\text{th}}(t) + b_{\text{coal}} \Delta t \quad (2)$$

where $M_{\text{coal,base}}(t)$ denotes the baseline coal consumption under pure-coal operation corresponding to the current thermal power output, in t; a_{coal} denotes the linear coal-consumption coefficient, in t/MWh; b_{coal} denotes the constant coal-consumption coefficient, in t/h; and Δt denotes the dispatch interval. In this study, a_{coal} = 0.274 t/MWh and b_{coal} = 18.246 t/h.

The ammonia co-firing ratio $\alpha(t)$ is defined as the fraction of ammonia heat input in the total fuel heat input from coal and ammonia. Accordingly, $\alpha(t)$ = 0.3 indicates that ammonia provides 30% of the total fuel heat input during the current dispatch interval. Because

coal and ammonia have different lower heating values (LHVs), their fuel substitution is modeled on an equal heat input basis. The variation in boiler efficiency caused by ammonia co-firing is neglected at the dispatch level. The required ammonia mass during the current dispatch interval is calculated as:

$$M_{\mathrm{NH_3}}(t) = M_{\mathrm{coal,base}}(t)\alpha(t)\frac{Q_{\mathrm{coal}}}{Q_{\mathrm{NH_3}}} \tag{3}$$

where $M_{\mathrm{NH_3}}(t)$ denotes the ammonia demand during the current dispatch interval, in t; Q_{coal} and $Q_{\mathrm{NH_3}}$ denote the lower heating values of coal and ammonia, respectively.

Under the equal heat input substitution assumption, the fraction of coal substituted by ammonia is represented by $\alpha(t)$. The actual coal consumption after ammonia co-firing is therefore expressed as:

$$M_{\mathrm{coal,act}}(t) = M_{\mathrm{coal,base}}(t)[1 - \alpha(t)] \tag{4}$$

where $M_{\mathrm{coal,act}}(t)$ denotes the actual coal consumption after coal–ammonia co-firing during dispatch interval t in t.

Equations (2)–(4) indicate that the actual coal consumption is jointly determined by thermal power output and the ammonia co-firing ratio.

Variations in wind energy alter the system power deficit and consequently require adjustments in thermal power output, which affect the baseline coal consumption. Meanwhile, hydrogen availability constrains the upper limit of the ammonia co-firing ratio. Therefore, the final coal consumption is determined by the combined effects of thermal power output and ammonia substitution rather than the ammonia co-firing ratio alone.

The direct CO_2 emission factor of coal combustion is used to calculate the direct CO_2 emissions of thermal power units [29]. The CO_2 emission factor for coal combustion is calculated as:

$$EF_{\mathrm{coal}} = (1 - \mathrm{C}')\mathrm{C_{ar}} \times \frac{44}{12} \tag{5}$$

where EF_{coal} denotes the direct CO_2 emission factor of coal combustion, in $\mathrm{t/t_{coal}}$; the factor 44/12 converts carbon content into the corresponding CO_2 mass after combustion. C_{ar} denotes the carbon content of coal on an as-received basis; and C' denotes the fraction of unoxidized carbon. In this study, C_{ar} = 0.45 and C' = 0.01, resulting in:

$$EF_{\mathrm{coal}}=1.6335\mathrm{t/t_{coal}}$$

The direct CO_2 emissions from thermal power units during the current dispatch interval are calculated as:

$$\mathrm{CO_{2,direct}}(t) = EF_{\mathrm{coal}}\mathrm{M_{coal,act}}(t) \tag{6}$$

where $\mathrm{CO_{2,direct}}(t)$ denotes the direct CO_2 emissions from coal combustion in thermal power units during dispatch interval t, in t.

Following the principles of ISO 14044 for defining the goal and scope of life cycle assessment [30], the CO_2 emission accounting boundary is defined according to the objective of this study. This study focuses on the operational CO_2 emissions of the wind–hydrogen–ammonia coupled thermal power system during EMS operation. The accounting boundary includes direct CO_2 emissions from coal combustion in thermal power units and indirect CO_2 emissions associated with grid electricity purchases. Life-cycle emissions associated with equipment manufacturing and construction, coal mining and transportation, infrastructure development, and other upstream processes are excluded from the accounting boundary. Therefore, the CO_2 emissions calculated in this study represent operational emissions rather than the complete life-cycle carbon footprint of the system. Within this

accounting boundary, ammonia combustion is assumed to produce no direct CO_2 emissions because ammonia molecules contain no carbon atoms [31,32].

The emission boundary of the present study is limited to operational CO_2 emissions. NO_x, N_2O, ammonia slip, and other non-CO_2 emissions associated with coal–ammonia co-firing are not included in the EMS objective or CO_2 emission-reduction indicators. Therefore, the calculated CO_2 emission reduction should not be interpreted as a comprehensive environmental-performance assessment of ammonia co-firing.

Indirect CO_2 emissions from grid electricity purchases are determined based on the actual purchased electricity, which is defined as:

$$E_{\text{buy}}(t) = \max[E_{\text{grid}}(t),0] \tag{7}$$

The indirect CO_2 emissions associated with grid electricity purchases are calculated as:

$$CO_{2,\text{grid}}(t) = EF_{\text{grid}} E_{\text{buy}}(t) \tag{8}$$

where $CO_{2,\text{grid}}(t)$ denotes the indirect CO_2 emissions associated with grid electricity purchases, in t; EF_{grid} denotes the average grid CO_2 emission factor. In the baseline case, it is set to 0.6479 t/MWh, corresponding to the 2023 provincial average electricity CO_2 emission factor for Inner Mongolia; and $E_{\text{buy}}(t)$ denotes the purchased electricity from the grid, in MWh.

The system operational CO_2 emissions considered in the EMS optimization are expressed as:

$$CO_{2,\text{system}}(t) = CO_{2,\text{direct}}(t) + CO_{2,\text{grid}}(t) \tag{9}$$

where $CO_{2,\text{system}}(t)$ denotes the system operational CO_2 emissions during dispatch interval t, in t.

To separately evaluate the direct CO_2 emission reduction achieved through coal–ammonia substitution, the CO_2 emissions under pure-coal operation with the same thermal power output are also calculated as follows:

$$CO_{2,\text{coal}}(t) = EF_{\text{coal}} M_{\text{coal,base}}(t) \tag{10}$$

The above models establish the relationship between operating conditions and cumulative CO_2 emissions. Variations in wind energy profiles lead to corresponding changes in thermal power output and consequently affect baseline coal consumption under pure-coal operation. The amount of surplus wind energy and the hydrogen storage level also affect hydrogen production, hydrogen availability, and the achievable ammonia co-firing ratio, which further determine the amount of coal consumption reduced through ammonia substitution and the actual coal consumption. When indirect CO_2 emissions associated with grid electricity purchases are considered, these factors jointly determine the cumulative system CO_2 emissions under different operating conditions.

2.3. Hydrogen Production–Storage–Ammonia Synthesis Models and Dynamic Operating Constraints

2.3.1. Ammonia Synthesis, Electrolytic Hydrogen Production, and Hydrogen Storage Models

The ammonia synthesis system determines its electricity and hydrogen consumption according to the ammonia demand of thermal power units. The corresponding consumption can be described using the mass and energy balance equations of the power-to-

ammonia (P2A) system. The electrical energy required for ammonia synthesis is expressed as follows [33,34]:

$$E_{\text{wind,NH}_3}(t) = k_{ele,\text{NH}_3} M_{\text{NH}_3}(t) \tag{11}$$

The electricity-equivalent hydrogen requirement for ammonia synthesis is expressed as:

$$H_{\text{dem}}(t) = k_{\text{H}_2,\text{NH}_3} M_{\text{NH}_3}(t) \tag{12}$$

where k_{ele,NH_3} denotes the electricity consumption coefficient for ammonia synthesis; $k_{\text{H}_2,\text{NH}_3}$ denotes the electricity-equivalent coefficient associated with hydrogen production for ammonia synthesis and is set to 9.7 MWh/t based on the reported electricity consumption associated with electrolytic hydrogen production for green ammonia production [33]. $H_{\text{dem}}(t)$ denotes the electricity-equivalent hydrogen demand withdrawn from storage during dispatch interval t, in MWh. The coefficient of 9.7 MWh/t represents the electricity required for hydrogen production associated with one tonne of ammonia, rather than the chemical energy of hydrogen on a lower heating value (LHV) basis. Accordingly, the hydrogen storage state is expressed on an electricity-equivalent basis for dispatch-level accounting. Since this coefficient already represents the electricity consumption for hydrogen production, no additional electrolyzer efficiency factor is applied.

In this study, the ammonia synthesis subsystem is represented by an aggregated dispatch-level model. Its electricity and hydrogen requirements are determined according to the ammonia demand of the thermal power unit. Detailed equipment-level characteristics of the ammonia synthesis plant, including ammonia storage, synthesis capacity limits, minimum operating load, ramping constraints, and start-up/shutdown processes, are not explicitly modeled. This simplification is adopted because the present study focuses on the system-level coordination of wind energy, hydrogen production and storage, ammonia demand, and the operation of thermal power units, rather than on the detailed dynamic operation of the ammonia synthesis plant.

The electricity-equivalent increment credited to hydrogen storage during dispatch interval t is calculated as follows: [35]:

$$H_{\text{prod}}(t) = E_{\text{wind,H}_2}(t) \tag{13}$$

where $H_{\text{prod}}(t)$ denotes the electricity-equivalent increment credited to the hydrogen storage state during dispatch interval t, in MWh; and $E_{\text{wind,H}_2}(t)$ denotes the electricity allocated to electrolytic hydrogen production during the same interval, in MWh. Equation (13) represents an electricity-equivalent accounting relationship and does not imply a physical electrolyzer efficiency of 100%.

It should be noted that $k_{\text{H}_2,\text{NH}_3}$ represents the electricity-equivalent hydrogen demand coefficient associated with ammonia synthesis. Since hydrogen storage is expressed on an electricity-equivalent basis for dispatch-level accounting, this coefficient directly represents the electricity-equivalent hydrogen requirement corresponding to ammonia production.

To prevent the hydrogen storage level from exceeding its capacity limit, the wind energy allocated to electrolytic hydrogen production is constrained by three factors: available surplus wind energy, the maximum electricity input of the electrolyzer, and the remaining hydrogen storage capacity:

$$E_{\text{wind,H}_2}(t) = \min\{E_{\text{wind,sur}}(t), E_{\text{el,max}}, E_{\text{el,sto,max}}(t)\} \tag{14}$$

The maximum electrolyzer electricity input allowed by the remaining hydrogen storage capacity is calculated as:

$$E_{\mathrm{el,sto,max}}(t) = \max\{0, H_{\max} - H(t-1) + H_{\mathrm{dem}}(t)\} \tag{15}$$

where $E_{\mathrm{wind,sur}}(t)$ denotes the surplus wind energy remaining after satisfying the electricity demands of ammonia synthesis and the electrical load, in MWh; $E_{\mathrm{el,max}}$ denotes the maximum electricity input allowed for the electrolyzer within a single dispatch interval, in MWh; $E_{\mathrm{el,sto,max}}(t)$ denotes the maximum electrolyzer electricity input limited by the remaining hydrogen storage capacity, in MWh; $H_{\max}$ denotes the maximum electricity-equivalent hydrogen storage capacity, in MWh.; and $H(t-1)$ denotes the hydrogen storage level at the end of the previous dispatch interval, in MWh.

The hydrogen storage system is used to describe the dynamic evolution of the hydrogen storage level [36]. Its state update equation is expressed as:

$$\begin{cases} H(t) = H(t-1) - H_{\mathrm{dem}}(t) + H_{\mathrm{prod}}(t) \\ H_{\min} \le H(t) \le H_{\max} \end{cases} \tag{16}$$

where $H(t)$ denotes the hydrogen storage level at the end of dispatch interval t, $H_{\min}$ and $H_{\max}$ denote the lower and upper bounds of the hydrogen storage level, respectively.

The electricity-equivalent hydrogen storage variable is used only for dispatch-level state tracking and hydrogen-availability constraints. It does not represent the LHV-based chemical energy of hydrogen and is not directly converted into physical hydrogen mass or storage volume in this study.

The present study adopts a dispatch-level energy-flow model and does not explicitly model the pressure, temperature, or specific technology of the hydrogen storage system. Therefore, a fixed physical storage volume is not prescribed. The actual storage volume depends on the selected storage technology and its operating pressure and temperature. Hydrogen charging and discharging losses are neglected, while the electricity consumption associated with electrolytic hydrogen production is represented by the empirical coefficient of 9.7 MWh/t, without applying an additional electrolyzer efficiency factor.

2.3.2. Temporal Causality Constraint on Hydrogen Utilization

To avoid overestimating hydrogen availability when hydrogen production and ammonia synthesis occur within the same dispatch interval, a temporal causality constraint on hydrogen utilization is introduced into the EMS. Under this constraint, the hydrogen required for ammonia synthesis during the current dispatch interval can only be supplied by the hydrogen stored at the end of the previous dispatch interval [37]:

$$H_{\mathrm{dem}}(t) \le H(t-1) \tag{17}$$

Hydrogen produced by the electrolyzer during the current dispatch interval, $H_{\mathrm{prod}}(t)$, is used only to update the hydrogen storage level $H(t)$ at the end of that interval. It cannot be used to satisfy the hydrogen demand for ammonia synthesis within the same interval and becomes available only in subsequent dispatch intervals.

To illustrate the temporal causality constraint, consider a case in which the hydrogen storage level at the end of the previous dispatch interval is $H(t-1)$ = 100 MWh, while 40 MWh of hydrogen storage-state increment is produced by electrolysis during the current dispatch interval. Suppose that a candidate dispatch solution requires $H_{\mathrm{dem}}(t)$ = 120 MWh for ammonia synthesis. Without the temporal causality constraint on hydrogen utilization, directly combining the newly produced hydrogen with the hydrogen stored at the end

of the previous dispatch interval would result in 140 MWh of available hydrogen, and the candidate solution would be incorrectly considered feasible. Under the temporal causality constraint, only the 100 MWh stored at the end of the previous dispatch interval is available for ammonia synthesis in the current interval. Therefore, the candidate solution with $H_{\mathrm{dem}}(t)$ = 120 MWh is infeasible. The EMS must reduce the ammonia co-firing ratio until the hydrogen demand satisfies $H_{\mathrm{dem}}(t) \leq H(t-1)$. The 40 MWh produced during the current dispatch interval is first stored in the hydrogen storage system and becomes available for ammonia synthesis only in subsequent dispatch intervals.

In practical renewable-energy-based hydrogen production systems, an intermediate hydrogen storage stage is commonly used to buffer fluctuations in electrolytic hydrogen production and provide a stable hydrogen supply for subsequent ammonia synthesis [38]. The "storage-before-utilization" mechanism adopted in this study provides a discrete representation of this physical operating sequence at a dispatch resolution of 0.5 h. The 0.5 h interval represents only the EMS dispatch and system-state update resolution. Accordingly, the one-interval separation does not represent a prescribed 0.5 h physical delay associated with hydrogen storage, compression, transportation, or ammonia-synthesis processing, but rather the temporal availability boundary defined by the discrete state-update sequence.

2.3.3. Dispatch-Level Dynamic Ammonia Co-Firing Constraints for Thermal Power Units

In addition to the temporal causality constraint on hydrogen utilization, the operational continuity of coal–ammonia co-firing units between consecutive dispatch intervals is considered. At the dispatch level, constraints on thermal power output variation, ammonia co-firing ratio adjustment, and the minimum stable output are imposed to maintain smooth transitions in unit operating states between consecutive intervals. These constraints support operational feasibility at the dispatch level. This study focuses on energy dispatch optimization of the multi-energy-flow coupled system. Detailed dynamics of the boiler combustion process and actuators are not explicitly modeled.

The current thermal power output is constrained by the technical operating limits of the unit and its ramping capability between consecutive dispatch intervals:

$$\begin{cases} E_{\mathrm{th}}^{\mathrm{low}}(t) = [E_{\mathrm{th}}^{\mathrm{min}}, E_{\mathrm{th}}(t-1) - \Delta E_{\mathrm{th}}^{\mathrm{ramp}}]_{\mathrm{max}} \\ E_{\mathrm{th}}^{\mathrm{high}}(t) = [E_{\mathrm{th}}^{\mathrm{max}}, E_{\mathrm{th}}(t-1) + \Delta E_{\mathrm{th}}^{\mathrm{ramp}}]_{\mathrm{min}} \end{cases} \tag{18}$$

The resulting feasible range of thermal power output is expressed as:

$$E_{\mathrm{th}}^{\mathrm{low}}(t) \leq E_{\mathrm{th}}(t) \leq E_{\mathrm{th}}^{\mathrm{high}}(t) \tag{19}$$

where $E_{\mathrm{th}}^{\mathrm{low}}(t)$ denotes the dynamically feasible lower bound of thermal power output during dispatch interval t, in MWh; $E_{\mathrm{th}}^{\mathrm{high}}(t)$ denotes the corresponding dynamically feasible upper bound; $E_{\mathrm{th}}^{\mathrm{min}}(t)$ denotes the technical minimum output expressed on a dispatch-interval energy basis; and $E_{\mathrm{th}}^{\mathrm{max}}(t)$ denotes the maximum allowable thermal power output of the thermal power unit.

To avoid excessively rapid changes in the ammonia co-firing ratio during normal operation, an adjustment-rate constraint R_{α} is introduced. The feasible range of the ammonia co-firing ratio is expressed as:

$$\max[0, \alpha(t-1) - \mathrm{R}_{\alpha}\Delta t] \leq \alpha(t) \leq \min[\alpha_{\mathrm{max}}, \alpha(t-1) + \mathrm{R}_{\alpha}\Delta t] \tag{20}$$

where $\alpha(t)$ and $\alpha(t-1)$ denote the ammonia co-firing ratios during the current and previous dispatch intervals, respectively; α_{max} denotes the maximum allowable ammonia co-firing ratio; and $R\alpha$ denotes the ammonia co-firing ratio adjustment rate. In this study,

R_α = 0.3 h^{-1}, corresponding to a maximum change of 0.15 between two consecutive 0.5 h dispatch intervals under normal operation.

Existing studies have not established a unified quantitative relationship between the ammonia co-firing ratio and the minimum allowable thermal power output that can be directly applied to the system-level dispatch model considered in this study [17,39,40]. To represent the effect of the ammonia co-firing ratio on the low-load operating limit at the dispatch level, a linear coupling formulation is introduced between the ammonia co-firing ratio and the minimum allowable thermal power output:

$$\begin{cases} E_{\text{th}}^{\min}(\alpha, t) = E_{\text{th}}^{\min}[1 + k_\alpha \cdot \alpha(t)] \\ E_{\text{th}}(t) \geq E_{\text{th}}^{\min}(\alpha, t) \end{cases} \tag{21}$$

where $E_{\text{th}}^{\min}(\alpha, t)$ denotes the minimum allowable thermal power output considering the current ammonia co-firing ratio, and k_α denotes the dispatch-level coupling coefficient used to characterize the variation in the low-load operating limit. In this study, k_α is set to 0.25. This value is treated as a calibrated parameter in the dispatch model and is used to define the boundary of the feasible operating region as the ammonia co-firing ratio varies. It is not directly fitted to experimental data from a specific thermal power unit.

For example, when $E_{\text{th}}^{\min}$ = 60 MWh/interval and α = 0.3:

$$E_{\text{th}}^{\min}(0.30) = 60 \times (1 + 0.25 \times 0.30) = 64.5 \text{ MWh/interval}$$

At an ammonia co-firing ratio of 30%, the minimum allowable thermal power output in the model increases from 60 to 64.5 MWh/interval. This relationship is introduced to represent the operating boundary in system-level dispatch and should not be interpreted as an empirical correlation for the actual minimum stable output of a specific boiler. Its purpose is to avoid treating thermal power output and the ammonia co-firing ratio as completely independent decision variables and to preserve their necessary operational coupling within the feasible operating region.

As the hydrogen storage level approaches depletion, the hydrogen demand for ammonia synthesis may still exceed the hydrogen stored at the end of the previous dispatch interval, even when the ammonia co-firing ratio has been reduced to the minimum value allowed by the normal downward adjustment-rate constraint in Equation (20). Enforcing this adjustment-rate constraint under such conditions may result in the absence of a feasible operating point that satisfies the hydrogen availability requirement for the current dispatch interval. Therefore, a hydrogen-availability-based emergency reduction mechanism for the ammonia co-firing ratio is introduced.

If the minimum ammonia co-firing ratio allowed by the normal downward adjustment-rate constraint still violates the hydrogen availability constraint in Equation (17), the EMS relaxes the normal downward adjustment-rate constraint and extends the lower bound of the ammonia co-firing ratio to zero. The operating point is then re-optimized within the expanded feasible range rather than directly setting the ammonia co-firing ratio to zero. Only when the available hydrogen is insufficient to support any ammonia co-firing is α = 0 permitted, in which case the thermal power unit temporarily switches to pure-coal operation during the current dispatch interval.

2.4. Interval-by-Interval EMS Optimization Based on Multi-Objective PSO

2.4.1. Decision Variables and Multi-Objective Function

A discrete-time interval-by-interval EMS optimization framework with a 0.5 h dispatch interval is adopted in this study [41]. At each dispatch interval, only the operating point of the current interval is optimized based on the current wind energy, load demand, and sys-

tem states inherited from the previous interval. After the operating point is determined, the system states are updated and passed to the next dispatch interval, where the optimization procedure is repeated. No future prediction horizon or multi-interval objective function is introduced; inter-interval coupling is represented through the inherited system states and dynamic operating constraints.

The EMS decision vector is defined as:

$$\mathbf{x}(t) = [E_{\text{th}}(t), \alpha(t)] \tag{22}$$

The corresponding EMS input vector is:

$$\boldsymbol{u}(t) = [E_{\text{wind}}(t), E_{\text{load}}(t), H(t-1), \Delta E_{\text{th}}^{\text{ramp}}, E_{\text{th}}(t-1), \alpha(t-1)] \tag{23}$$

The EMS output vector is:

$$\mathbf{y}(t) = [E_{\text{th}}(t), \alpha(t), E_{\text{grid}}(t), E_{\text{wind,H}_2}(t), E_{\text{wind,NH}_3}(t)] \tag{24}$$

To coordinate low-carbon operation, grid electricity purchases, and thermal power output smoothing, a multi-objective fitness function is constructed within the EMS [42]. The fitness function consists of a CO_2 emission term, a grid electricity purchase penalty term, and a thermal power output ramping penalty term.

(1) Low-Carbon Objective

The carbon-emission objective is expressed as:

$$J_{\text{CO}_2}(t) = W_{\text{CO}_2} \frac{\text{CO}_{2,\text{system}}(t)}{\text{CO}_{2,\text{ref}}} \tag{25}$$

where W_{CO_2} denotes the weighting coefficient of the CO_2 emission objective, and $\text{CO}_{2,\text{system}}(t)$ denotes the system operational CO_2 emissions during dispatch interval t.

The reference CO_2 emission is defined as:

$$\text{CO}_{2,\text{ref}} = EF_{\text{coal}}(a_{coal} E_{\text{th}}^{\max} + b_{\text{coal}} \Delta t) = 82.04 \tag{26}$$

Here, $\text{CO}_{2,\text{ref}}$ denotes the reference value used to normalize the carbon-emission term and is set to 82.04 t/interval. It corresponds to the CO_2 emissions under pure-coal operation at the maximum allowable thermal power output.

(2) Grid Electricity Purchase Objective

The grid electricity purchase objective is expressed as:

$$J_{\text{buy}}(t) = W_{\text{buy}} \left[\frac{E_{\text{buy}}(t)}{E_{\text{buy,ref}}(t)} \right]^2 \tag{27}$$

where the reference value for grid electricity purchases is defined as:

$$E_{\text{buy,ref}}(t) = \max[E_{\text{load}}(t), 1] \tag{28}$$

Here, $E_{\text{buy,ref}}$ denotes the reference value used to normalize grid electricity purchases and is determined from the load demand during the current dispatch interval. When $E_{\text{load}}(t) < 1$ MWh, the reference value is set to 1 MWh to avoid numerical instability.

(3) Thermal Power Output Smoothing Objective

The thermal power output smoothing objective is expressed as:

$$J_{\text{ramp}}(t) = W_{\text{ramp}} \cdot \left(\frac{E_{\text{th}}(t) - E_{\text{th}}(t-1)}{E_{\text{ramp,ref}}} \right)^2 \tag{29}$$

where $E_{\text{ramp,ref}}$ denotes the reference value used to normalize the variation in thermal power output between consecutive dispatch intervals. Under normal operating conditions, it is set to the specified maximum allowable change in thermal power output. When $E_{\text{ramp,ref}}$ approaches zero, it is set to 1 MWh to avoid division by zero.

(4) Overall Fitness Function

Based on the above objectives, the overall EMS fitness function is formulated as:

$$J = J_{\text{CO2}} + J_{\text{buy}} + J_{\text{ramp}} \tag{30}$$

The weighting coefficients W_{CO_2}, W_{buy} and W_{ramp} are set to 1.0×10^5, 1.0×10^3, 1.0×10^2, respectively.

All three objective terms are normalized before weighting. The weighting coefficients therefore represent their relative priorities in the EMS optimization. With the selected weighting scheme, CO_2 emission reduction is given the highest priority, followed by limiting grid electricity purchases, while thermal power output smoothing is treated as an auxiliary objective. The influence of different weighting settings on EMS operation is further examined through sensitivity analysis.

Key physical constraints are not treated solely as additional penalty terms in the objective function. The EMS first performs a hard feasibility check for constraints including the dynamically feasible operating region of thermal power units, minimum stable output, temporal hydrogen availability, hydrogen storage capacity, and grid electricity exchange capacity. Candidate solutions that violate these constraints are assigned a large penalty value and excluded from the normal fitness comparison. This procedure allows the final PSO solution to be selected from feasible candidate solutions that satisfy the dispatch-level operating constraints.

2.4.2. Interval-by-Interval Solution Process Based on PSO

PSO is adopted to solve the nonlinear optimization problem for each dispatch interval [43,44]. Thermal power output and the ammonia co-firing ratio constitute the two primary decision variables. Although only two decision variables are optimized in each dispatch interval, the EMS problem is not a simple two-dimensional unconstrained optimization problem. These variables are coupled with hydrogen availability, ammonia co-firing ratio limits, the dynamic operating constraints of thermal power units, ramping constraints, and power balance requirements, resulting in a highly nonlinear and constrained feasible region. Therefore, PSO is employed due to its simple structure and capability to solve nonlinear constrained optimization problems.

At iteration k, the position of particle i represents a candidate operating solution:

$$\mathbf{x}_i^k = \left[E_{\text{th},i}^k, \alpha_i^k \right]^T \tag{31}$$

The particle velocity is updated as:

$$\mathbf{v}_i^{k+1} = w^k \mathbf{v}_i^k + c_1 r_1 \left(p_i^k - x_i^k \right) + c_2 r_2 \left(g^k - x_i^k \right) \tag{32}$$

and the particle position is subsequently updated as:

$$\mathbf{x}_i^{k+1} = \mathbf{x}_i^k + \mathbf{v}_i^{k+1} \tag{33}$$

Here p_i^k denotes the personal-best position of particle i up to iteration k; g^k denotes the global-best position of the swarm at iteration k; r_1 and r_2 denote independent random variables uniformly distributed over [0,1]; and c_1, c_2 denote the cognitive and social acceleration coefficients, respectively. Both acceleration coefficients are set to 1.49 in this study.

The swarm size and maximum number of iterations are both set to 20. The inertia weight decreases linearly from 0.90 to 0.40 over the optimization process, allowing greater exploration during the early iterations and more localized search during the later iterations. The maximum particle velocity in each decision dimension is limited to 20% of the width of the corresponding search range.

For comparison, the GA was implemented using the same EMS model, objective function, and constraint conditions as the PSO. The population size and maximum generation number were set to 20 and 20, respectively, resulting in the same computational budget (400 candidate evaluations) as PSO. Tournament selection, arithmetic crossover (P_c = 0.8), Gaussian mutation (P_m = 0.1), and an elitism strategy were adopted.

At each dispatch interval, the PSO search bounds are first determined based on the dynamic operating constraints of the thermal power unit and the ammonia co-firing ratio adjustment constraint. When the hydrogen-availability-based emergency reduction mechanism described in Section 2.3.3 is triggered, the lower bound of the ammonia co-firing ratio is reduced to zero before the PSO search begins. Candidate solutions are then checked against the operating constraints and the temporal causality constraint on hydrogen utilization. Feasible candidates are subsequently evaluated using the fitness function, followed by iterative particle updates to obtain the optimal operating point for the current dispatch interval. The overall interval-by-interval optimization and constraint-checking process is illustrated in Figure 2.

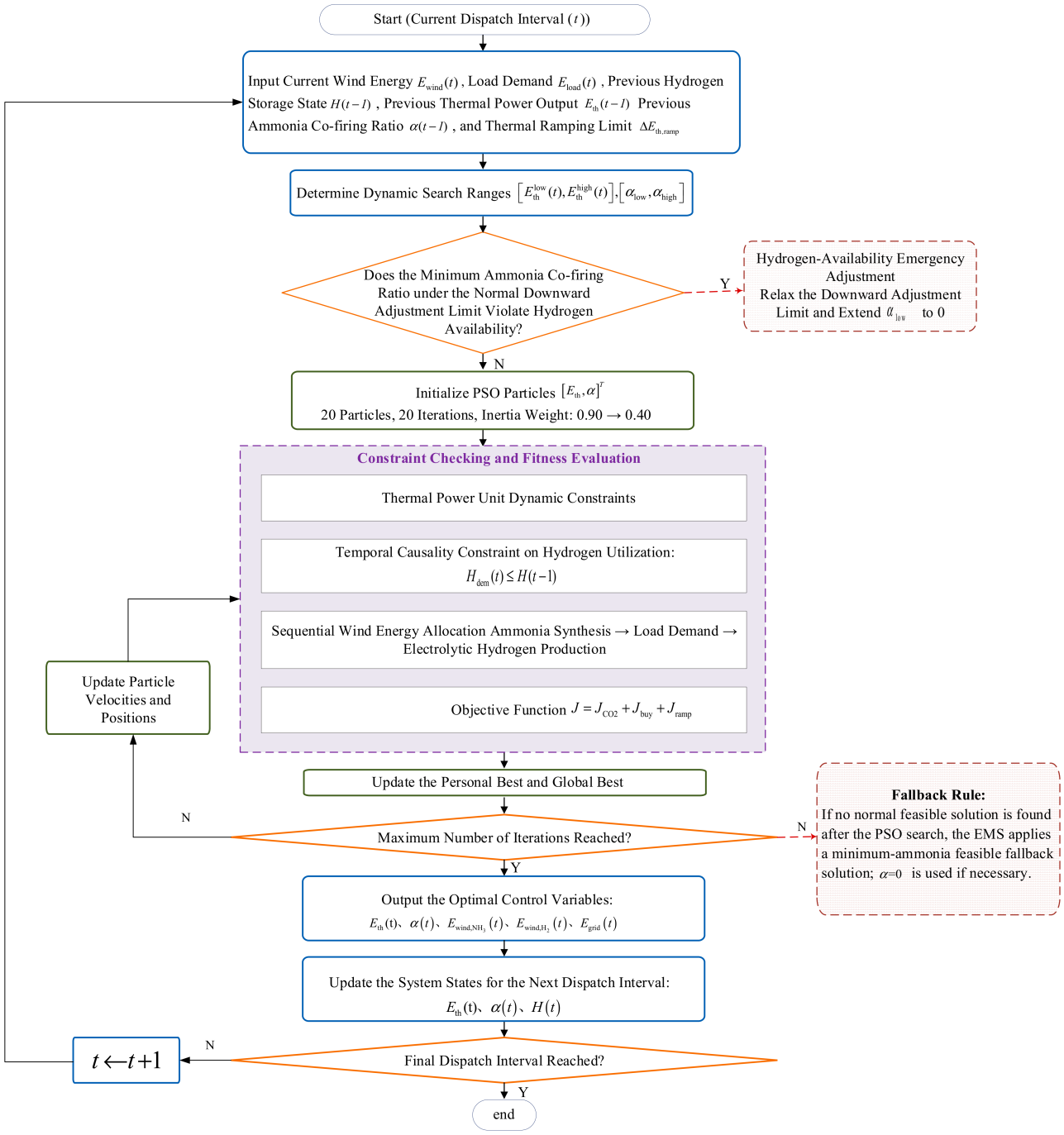


Figure 2. Interval-by-interval EMS optimization and constraint-checking process based on multi-objective PSO.

3. Case Study and Simulation Data

3.1. Data Sources and System Parameters

The simulation model is developed in MATLAB/Simulink R2023a, with the EMS dispatch interval set to 0.5 h. The main parameters of the system model and PSO are listed in Table 1. Parameters related to coal consumption of thermal power units, electrolytic hydrogen production, and ammonia synthesis are adopted from the relevant literature. The ammonia co-firing ratio adjustment rate and the coupling coefficient between the ammonia co-firing ratio and the minimum allowable thermal power output are treated as calibrated parameters in the dispatch model. The baseline values of the multi-objective weights are determined based on the parameter sensitivity analysis. This study focuses on the

operational control strategy under predefined equipment capacities. Capacity optimization of the electrolyzer, hydrogen storage system, and thermal power units is beyond the scope of this study.

Table 1. Main parameters of the system model and the PSO algorithm.

Parameter	Numerical Value	Unit	Reference	Description
Δt	0.5	h	-	Dispatch interval
E_{th}^{min}	60	MWh	-	Minimum thermal power output
E_{th}^{max}	150	MWh	-	Maximum thermal power output
ΔE_{th}^{ramp}	50	MWh	-	Maximum allowable change in thermal power output between adjacent dispatch intervals
H_{min}	0	MWh	-	Minimum hydrogen storage level
H_{max}	5000	MWh	-	Maximum hydrogen storage level
H_0	1000	MWh	-	Baseline initial hydrogen storage level
$E_{el,max}$	400	MWh	-	Maximum electrolyzer electricity input
$E_{grid,buy,max}$	400	MWh	-	Maximum grid electricity purchase
$E_{grid,sell,max}$	400	MWh	-	Maximum grid electricity sale
a_{coal}	0.274	t/MWh	[28]	Linear coefficient of coal consumption
b_{coal}	18.246	t/h	[28]	Constant coal consumption coefficient
k_{ele,NH_3}	0.6	MWh/t	[33]	Electricity consumption coefficient for ammonia synthesis
k_{H_2,NH_3}	9.7	MWh/t	[33]	Electricity-equivalent hydrogen demand coefficient for ammonia synthesis
EF_{grid}	0.6479	t/MWh	[45]	Grid CO_2 emission factor
EF_{coal}	1.6335	t/t_{coal}	-	Coal CO_2 emission factor
R_α	0.30	h^{-1}	-	Ammonia co-firing ratio adjustment rate
Q_{coal}	29,307.6	kJ/kg	-	Lower heating value of coal
Q_{NH_3}	18,602.9	kJ/kg	-	Lower heating value of ammonia
α_{max}	0.3	-	-	Maximum ammonia co-firing ratio
k_α	0.25	-	-	Coupling coefficient between ammonia co-firing ratio and minimum allowable thermal power output
W_{CO_2}	10^5	-	-	CO_2 emission objective weight
W_{buy}	10^3	-	-	Grid electricity purchase objective weight
W_{ramp}	10^2	-	-	Thermal power output ramping objective weight
N_p	20	-	-	Number of particles
K_{max}	20	-	-	Maximum number of iterations
C'	0.01	-	[46]	Unoxidized carbon fraction
C_{ar}	0.45	-	[46]	As-received elemental carbon content of coal
ω	0.9–0.40	-	[47]	PSO inertia weight
c_1	1.49	-	[47]	Cognitive learning factor
c_2	1.49	-	[47]	Social learning factor
v_{max}	20% of the corresponding search-range width		-	Maximum particle velocity

For reproducibility, a fixed random seed of 20260829 was used in the baseline simulations. Unless otherwise specified, the initial hydrogen storage level, thermal power output, and ammonia co-firing ratio were set to 1000 MWh, 60 MWh/interval, and 0, respectively. The maximum allowable change in thermal power output between two consecutive dispatch intervals was set to 50 MWh/interval.

Actual wind power data from a wind farm in Bayannur, Inner Mongolia, are used in this study. The original dataset covers the period from November 2023 to November 2024 with a sampling interval of 10 min. The data are resampled by averaging to a uniform

30 min temporal resolution, consistent with the 0.5 h EMS dispatch interval. Because the original wind data are recorded as power in MW, they are converted into wind energy before being used in the scheduling model. Specifically, the 30 min average wind power is multiplied by 0.5 h to obtain the wind energy for each dispatch interval, expressed in MWh/interval.

Owing to the limited availability of year-round measured load data, a 48-point measured daily load profile corresponding to the wind farm is used as the baseline intraday load pattern. Monthly seasonal factors, weekday/weekend adjustments, and holiday corrections are introduced to represent variations in load levels across different days. A zero-mean relative random perturbation with a standard deviation of 1.2% is further applied to avoid identical load profiles for days of the same type. Based on these adjustments, a synthetic annual load series with a temporal resolution of 0.5 h is constructed. The random perturbation represents only small intraday variations, while the main temporal variations in the annual load profile are determined by seasonal, weekday/weekend, and holiday adjustment factors. The synthetic load series is primarily used to evaluate the EMS under year-round continuous operation and inter-day carryover of the hydrogen storage state. Wind energy and load demand are selected as the two principal time-varying external inputs because their matching relationship determines the energy surplus or deficit in each dispatch interval, thereby affecting thermal power output and the surplus wind energy available for electrolytic hydrogen production.

3.2. Typical-Day Selection and Year-Round Simulation Settings

To evaluate EMS operation under different seasonal and wind–load matching conditions, three representative operating scenarios are defined based on the relative wind power level and intraday variability: the high-volatility disturbance day, thermal-power-support day, and surplus-hydrogen-storage day. One day from each scenario is selected for each season, resulting in nine typical days in total.

The high-volatility disturbance day is characterized by pronounced intraday variations in wind power, causing the system to switch frequently between wind power deficit and surplus conditions. This scenario is used to evaluate the coordinated responses of thermal power output, the hydrogen storage level, and the ammonia co-firing ratio to wind power fluctuations. The thermal-power-support day represents conditions in which wind power remains insufficient to meet the load demand over an extended period, requiring thermal power units to provide sustained power support. The surplus-hydrogen-storage day is characterized by abundant wind power. After the main system electricity demand is satisfied, substantial surplus wind energy remains available for electrolytic hydrogen production and storage, increasing hydrogen availability for sustained coal-ammonia co-firing. The wind–load profiles of the three representative operating scenarios are shown in Figure 3.

In this study, the seasonal classification follows the climatic characteristics of Inner Mongolia, China. Considering the prolonged cold period and heating season in this region, late March is still categorized as a winter operating period for the representative-day selection.

For the year-round simulation, a 365-day continuous simulation is conducted using the same 0.5 h dispatch resolution. The initial hydrogen storage level is set to 1000 MWh. The hydrogen storage state is continuously carried over between consecutive dispatch intervals and across consecutive days without a daily reset. Equipment capacities, operating constraints, and the CO_2 emission accounting boundary are kept consistent with those used in the typical-day simulations. The annual wind power and load profiles used for the year-round simulation are shown in Figure 4.

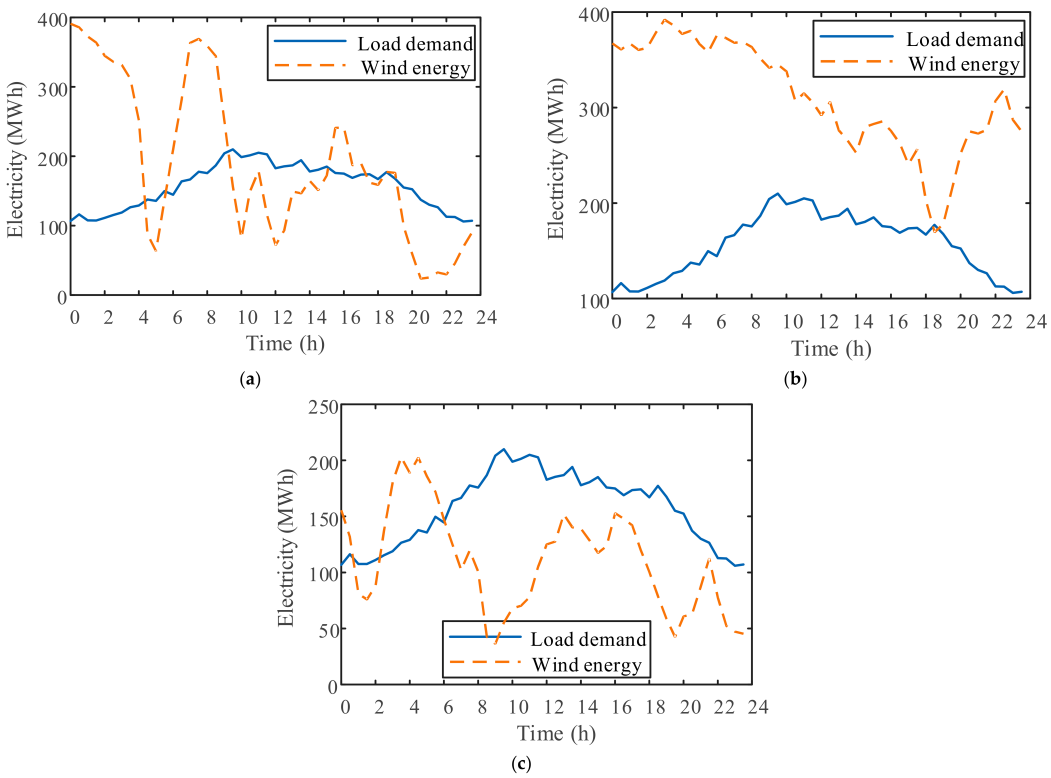


Figure 3. Wind energy and load demand under three representative days: (**a**) late-winter high-volatility disturbance day, 30 March 2024; (**b**) summer surplus-hydrogen-storage day, 27 July 2024; (**c**) transition-season thermal-power-support day, 22 April 2024.

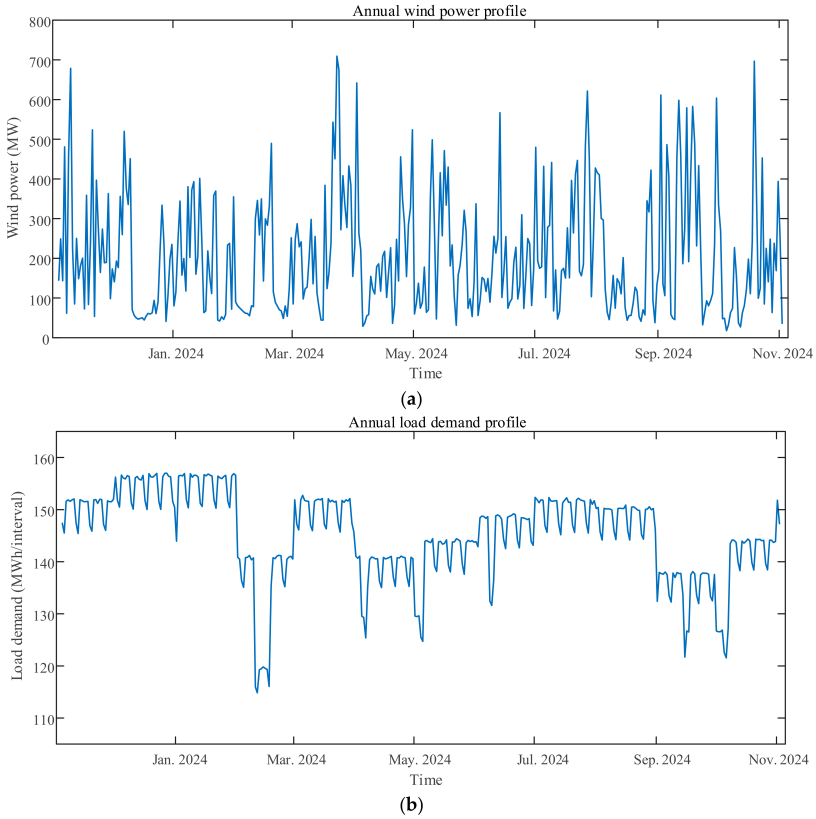


Figure 4. Annual input profiles used for the year-round simulation: (**a**) wind power; (**b**) load demand. The displayed profiles are daily averages derived from the original 30-min input series for improved readability at the annual scale.

3.3. Comparative Experiments and Sensitivity Analysis Settings

To evaluate the reasonableness of the key parameter settings and the operating performance of the PSO-based EMS, multi-objective weight sensitivity analysis, initial hydrogen storage level sensitivity analysis, and comparisons among different EMS solution methods are conducted. Except for the parameter or solution method under investigation, the system model, equipment capacities, input data, operating constraints, and carbon emission accounting boundary are kept identical across all cases.

3.3.1. Settings for Multi-Objective Weight Sensitivity Analysis

The objective function includes three terms associated with system operational CO_2 emissions, grid electricity purchases, and thermal power output smoothing. To reduce the subjectivity associated with weight selection, a one-at-a-time (OAT) approach is adopted for the sensitivity analysis. Only one objective weight is varied at a time, while the other two are maintained at their baseline values. The thermal-power-support day is selected as the common test scenario. Each of the three weights is varied over several orders of magnitude to examine the resulting changes in system CO_2 emissions, grid electricity purchases, hydrogen production, thermal power output, and ramping characteristics.

The effects of W_{CO_2} are examined to assess the priority assigned to the CO_2 emission objective, while W_{buy} reflects the relative emphasis placed on limiting grid electricity purchases. W_{ramp} is used to evaluate the trade-off between thermal power output smoothing and low-carbon system operation.

For W_{ramp} in addition to overall operating indicators such as system CO_2 emissions and grid electricity purchases, thermal power output trajectories and mean absolute ramping magnitudes under different weight settings are compared to characterize changes in thermal power output smoothing. The one-at-a-time sensitivity analysis described above is used to compare changes in system operation under different weight settings. Based on the analysis, $W_{CO_2} = 10^5$, $W_{buy} = 10^3$, and $W_{ramp} = 10^2$ are selected as the baseline weight combination for subsequent simulations. The corresponding results and their effects on system operation are further analyzed in Section 4.

3.3.2. Initial Hydrogen Storage State Sensitivity Analysis Settings

The initial hydrogen storage level determines the amount of stored hydrogen available at the beginning of the simulation. In the dispatch model, hydrogen storage is represented by the MWh-based storage variable used for dispatch-level state tracking. Seven initial hydrogen storage levels of 0, 250, 500, 1000, 2000, 3000, and 5000 MWh are considered. Independent simulations are conducted for the winter high-volatility disturbance day, summer surplus-hydrogen-storage day, and transition-season thermal-power-support day.

This sensitivity analysis is not intended for capacity optimization of the hydrogen storage system. The maximum hydrogen storage capacity is fixed at 5000 MWh in all cases, while only the initial hydrogen storage level is varied. An initial hydrogen storage level of 1000 MWh is adopted for the subsequent baseline cases, and its reasonableness is assessed through the multi-scenario sensitivity analysis described above. This setup clearly distinguishes the hydrogen storage capacity from the initial hydrogen storage level and avoids confusion between initial-level sensitivity analysis and capacity optimization.

3.3.3. Comparative Settings for Different EMS Algorithms

To evaluate the optimization performance of PSO for the interval-by-interval EMS scheduling problem considered in this study, the single-step baseline method and GA are selected as benchmark methods for comparison with the PSO-based EMS. The comparison is conducted under the same three representative operating scenarios: the winter high-

volatility disturbance day, summer surplus-hydrogen-storage day, and transition-season thermal-power-support day.

During the comparison, wind energy and load inputs, equipment parameters, initial hydrogen storage level, operating constraints of thermal power units, the temporal causality constraint on hydrogen utilization, and the CO_2 emission accounting method are kept identical across all methods. This setup reduces the influence of non-algorithmic factors on the comparison results. The main performance indicators include system operational CO_2 emissions, the system CO_2 emission reduction rate, the average ammonia co-firing ratio, and grid electricity purchases.

PSO serves as the primary optimization method for the proposed EMS. GA is included as another population-based optimization algorithm for the same scheduling problem. The single-step baseline method is implemented as a deterministic rule-based dispatch strategy without population-based search. In this method, the ammonia co-firing ratio is determined according to the previous hydrogen storage level, while thermal power output tracks the net load within the dynamically feasible operating range. All three methods are evaluated under the same typical-day conditions, and the comparative results are presented in Section 4.

4. Simulation Analysis

4.1. System Operating Characteristics Under Different Typical Conditions

To analyze EMS operation under different seasonal and wind–load matching conditions, three representative days are selected from the nine typical days for detailed analysis: the winter high-volatility disturbance day, summer surplus-hydrogen-storage day, and transition-season thermal-power-support day.

4.1.1. Winter High-Volatility Disturbance Day

As shown in Figure 5, under this condition, wind power exhibits pronounced intraday fluctuations, and thermal power output is dynamically adjusted according to the wind–load matching condition. When available wind power decreases, thermal power units increase their output to maintain the system power balance. During intervals with relatively abundant wind energy, the hydrogen storage level is replenished. The ammonia co-firing ratio is adjusted according to the hydrogen storage level and gradually decreases when hydrogen availability becomes insufficient. This behavior reflects the constraint imposed by hydrogen availability on the achievable ammonia co-firing ratio. At the same thermal power output, the instantaneous coal consumption and CO_2 emissions under ammonia co-firing are generally lower than those under the pure-coal baseline.

The daily results show that, with an initial hydrogen storage level of 1000 MWh, the average ammonia co-firing ratio is 19.41%. Direct CO_2 emissions from thermal power units are 1809.54 t. After accounting for the indirect emissions associated with 14.29 MWh of grid electricity purchases, system operational CO_2 emissions increase to 1818.80 t. Compared with the pure-coal baseline of 2243.01 t under the same thermal power output trajectory, the CO_2 emission reduction rate is 18.91%. These results indicate that hydrogen storage enables intertemporal hydrogen utilization under fluctuating wind power conditions and supports coal–ammonia co-firing while satisfying the hydrogen availability constraint.

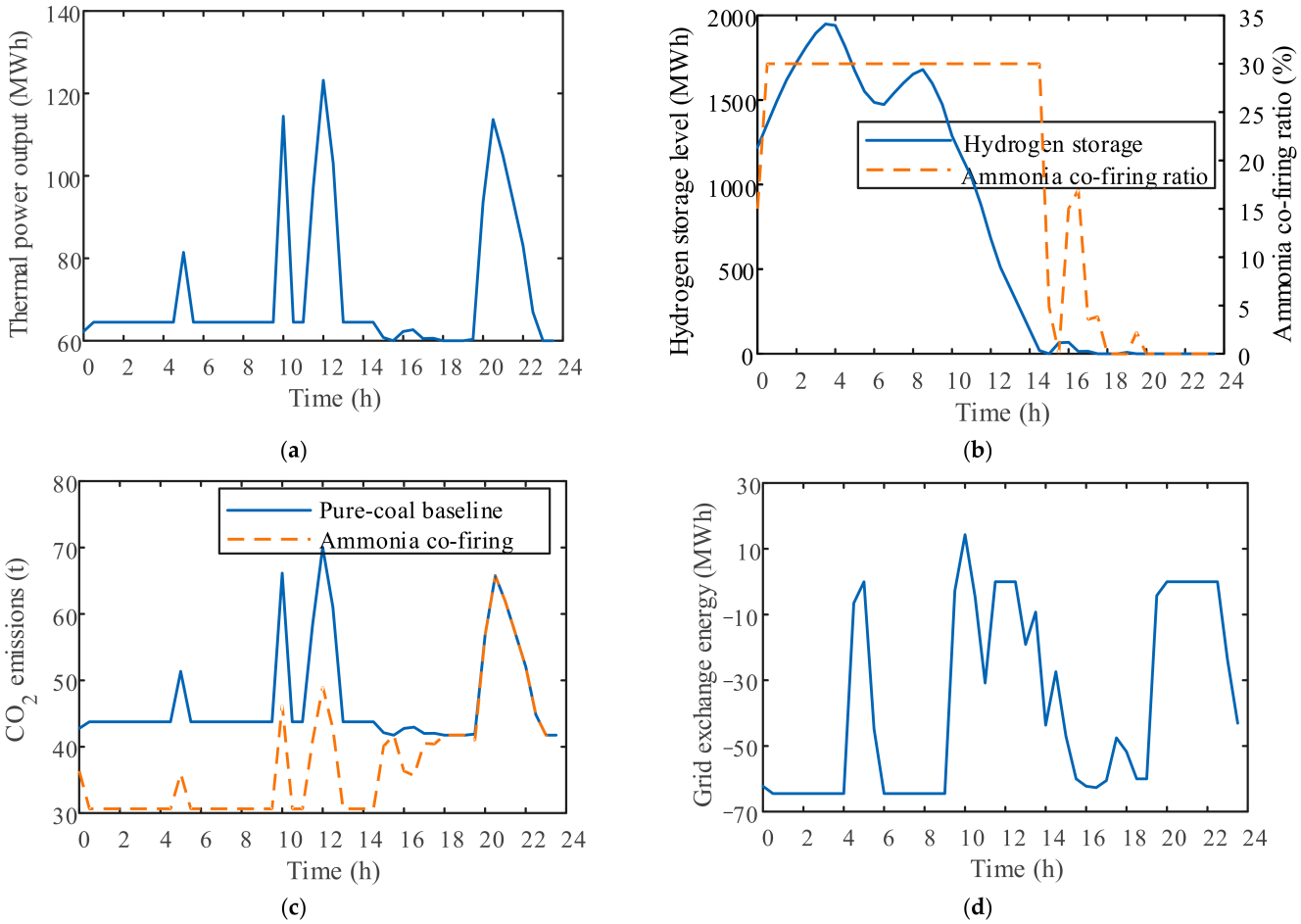


Figure 5. System operating results for the late-winter high-volatility disturbance day (30 March 2024). (**a**) Thermal power output; (**b**) Hydrogen storage level and ammonia co-firing ratio; (**c**) Comparison of carbon emissions; (**d**) Grid electricity exchange.

4.1.2. Summer Surplus-Hydrogen-Storage Day

As shown in Figure 6, the summer surplus-hydrogen-storage day is characterized by abundant wind energy. Wind energy remains relatively high during most dispatch intervals, reducing the need for grid electricity purchases. The hydrogen storage level also remains high, allowing the ammonia co-firing ratio to remain close to its maximum allowable value during most intervals. Thermal power units consequently operate mainly within a relatively low output range, while coal consumption and CO_2 emissions under ammonia co-firing are lower than those under pure-coal operation.

Both the direct CO_2 emissions from thermal power units and the system operational CO_2 emissions are 1476.42 t, with no grid electricity purchases during the day. Compared with the pure-coal baseline of 2100.01 t under the same thermal power output trajectory, the CO_2 emission reduction rate is 29.70%. The average ammonia co-firing ratio reaches 29.69%, close to the maximum allowable value of 30%. These results indicate that sufficient wind energy and hydrogen storage support a high ammonia co-firing ratio, resulting in greater coal substitution and CO_2 emission reduction.

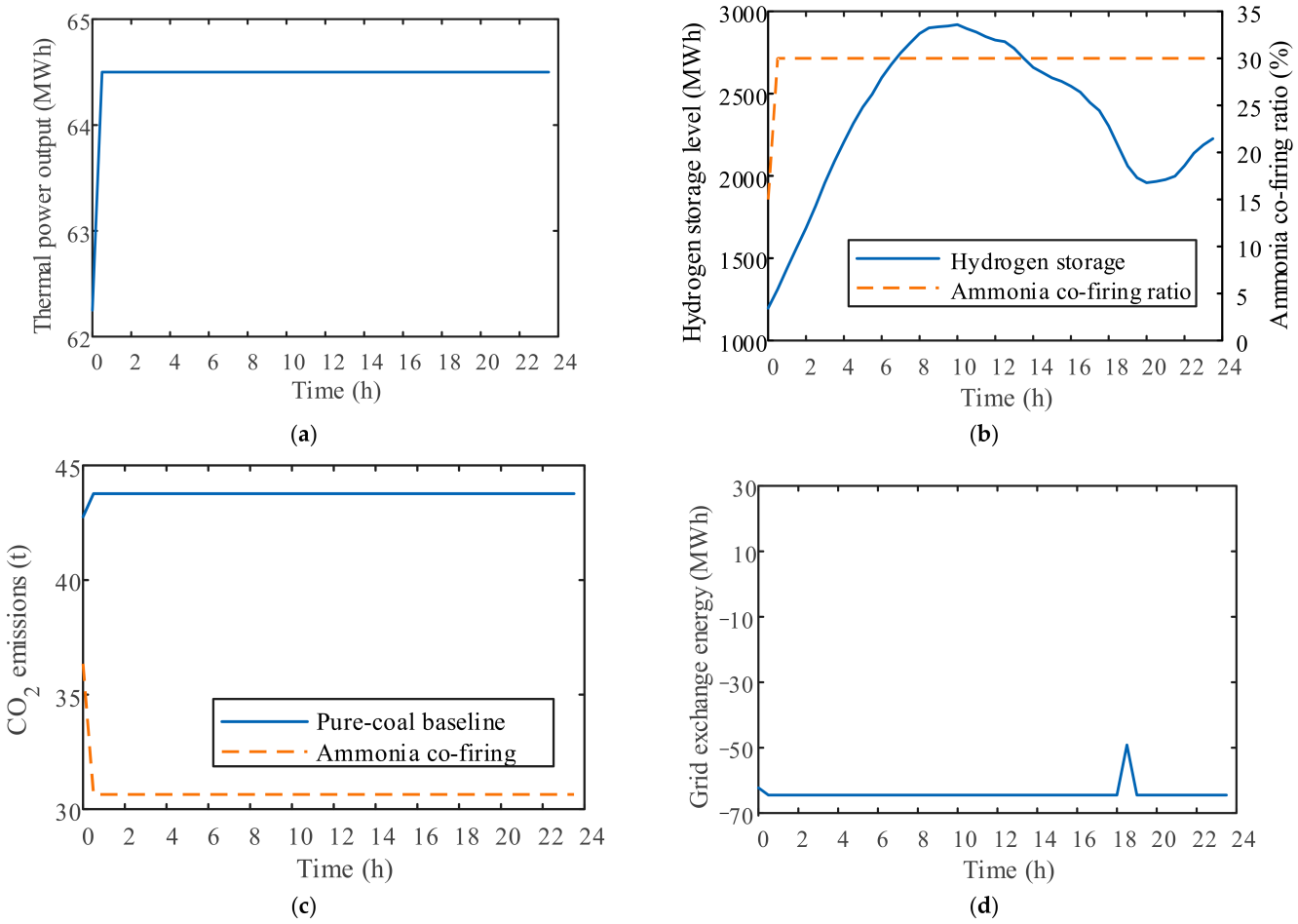


Figure 6. System operating results for the summer surplus-hydrogen-storage day (27 July 2024). (**a**) Thermal power output; (**b**) Hydrogen storage level and ammonia co-firing ratio; (**c**) Comparison of carbon emissions; (**d**) Grid electricity exchange.

4.1.3. Transition-Season Thermal-Power-Support Day

Figure 7 presents the operating results for the transition-season thermal-power-support day. During several dispatch intervals, the available wind energy is insufficient to meet the load demand. Thermal power units therefore provide additional power support, and thermal power output increases during intervals with insufficient wind energy. The hydrogen storage level declines throughout the day and reaches a relatively low level in the later intervals. The ammonia co-firing ratio decreases accordingly, indicating that limited hydrogen availability constrains the achievable ammonia co-firing ratio when sustained thermal power support is required.

The daily average ammonia co-firing ratio is 6.95%, and the direct CO_2 emissions from thermal power units are 2200.37 t. The system purchases 41.52 MWh of electricity from the grid. After accounting for the associated indirect emissions, system operational CO_2 emissions increase to 2227.27 t. Compared with the pure-coal baseline of 2345.97 t under the same thermal power output trajectory, the direct CO_2 emission reduction rate of the thermal power units is 6.21%, while the system CO_2 emission reduction rate is 5.060%. The difference between these two values indicates that indirect CO_2 emissions from grid electricity purchases offset part of the direct emission reduction achieved through coal–ammonia co-firing. Therefore, the evaluation of system-level low-carbon performance should account for both direct CO_2 emissions from coal combustion and indirect CO_2 emissions associated with grid electricity purchases.

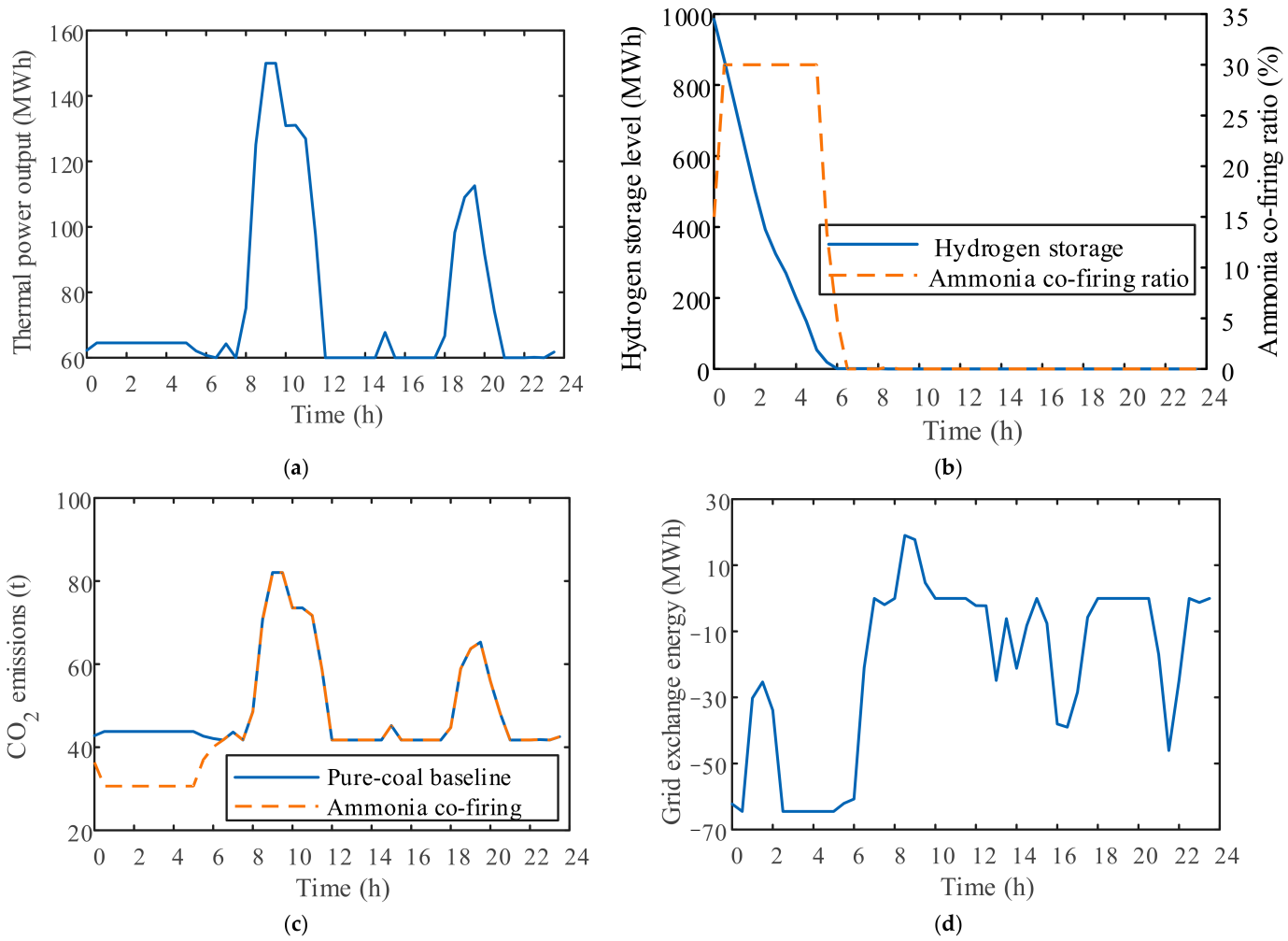


Figure 7. System operating results for the transition-season thermal-power-support day (22 April 2024). (**a**) Thermal power output; (**b**) Hydrogen storage level and ammonia co-firing ratio; (**c**) Comparison of carbon emissions; (**d**) Grid electricity exchange.

4.1.4. Comparison of Operating Characteristics Among the Three Typical Scenario Types

The pure-coal baseline is calculated from the thermal power output obtained in each scenario by assuming pure-coal combustion at the same thermal power output, rather than by performing a separate pure-coal dispatch simulation. Therefore, the baseline depends on the thermal power output rather than directly on the wind energy profile.

Table 2 shows distinct differences in system operation among the three representative scenario types. For the three surplus-hydrogen-storage days, the average ammonia co-firing ratio remains close to 0.30, with system CO_2 emission reduction rates of approximately 29.70%. For the high-volatility disturbance days, variations in wind energy and the hydrogen storage level result in system CO_2 emission reduction rates of approximately 18.91–25.07%. The thermal-power-support days exhibit lower average ammonia co-firing ratios because of limited surplus wind energy and hydrogen availability, with corresponding system CO_2 emission reduction rates of approximately 5.06–7.83%.

Table 2. Comparison of main operating indicators under nine typical-day scenarios.

Typical Scenario	CO_2 Emissions/t		System CO_2 Emission Reduction Rate/%	Average Ammonia Co-Firing Ratio/%	Grid Electricity Purchase/MWh
	Pure-Coal Baseline	System CO_2			
Late-winter high-volatility disturbance day	2243.01	1818.80	18.91	19.41	14.29
Late-winter surplus-hydrogen-storage day	2100.01	1476.42	29.70	29.69	0.00
Late-winter thermal-power-support day	2421.95	2232.24	7.83	7.99	12.18
Summer high-volatility disturbance day	2405.90	1802.80	25.07	25.44	17.45
Summer surplus-hydrogen-storage day	2100.01	1476.42	29.70	29.69	0.00
Summer thermal-power-support day	2295.05	2147.46	6.43	7.07	0.00
Transition-season high-volatility disturbance day	2268.53	1838.64	18.95	19.40	0.07
Transition-season surplus-hydrogen-storage day	2119.86	1490.32	29.70	29.69	0.00
Transition-season thermal-power-support day	2345.97	2227.27	5.06	6.95	41.52

Note: The pure-coal baseline CO_2 emissions are calculated under the same thermal power output trajectory as the proposed strategy. The CO_2 emission reduction rates are calculated based on the unrounded simulation results.

4.2. Parameter Sensitivity Analysis

4.2.1. Sensitivity Analysis of the Initial Hydrogen Storage Level

To assess the reasonableness of the baseline initial hydrogen storage level, seven initial hydrogen storage levels of 0, 250, 500, 1000, 2000, 3000, and 5000 MWh are considered. Simulations are conducted under the three representative operating scenarios. Only the initial hydrogen inventory is varied, while the maximum hydrogen storage capacity is fixed at 5000 MWh for all cases. The simulation results are shown in Table 3.

Figure 8 shows that increasing the initial hydrogen storage level generally enhances hydrogen availability and supports a higher ammonia co-firing ratio, thereby reducing system CO_2 emissions. This effect is more pronounced under the late-winter high-volatility disturbance and transition-season thermal-power-support conditions, whereas the summer surplus-hydrogen-storage case is less sensitive once sufficient hydrogen is available. Across the three cases, changes in system CO_2 emissions broadly follow those in the average ammonia co-firing ratio, indicating that increased hydrogen availability contributes to emission reduction by supporting greater ammonia utilization. When the initial storage level is very high, the remaining storage space for subsequent hydrogen production is reduced, as reflected by the lower electricity consumption for hydrogen production at 5000 MWh. This suggests that an excessively high initial storage level may limit the capacity to store newly produced hydrogen. Considering both initial hydrogen availability and the need to retain storage space for subsequent operation, 1000 MWh is adopted as the baseline initial hydrogen storage level in this study.

Table 3. System Operating Results under Different Initial Hydrogen Storage Levels.

Typical Scenario	Initial Hydrogen Storage/MWh	System CO_2 Emissions/t	Average Ammonia Co-Firing Ratio/%	Hydrogen Production Electricity Consumption/MWh	End-of-Day Hydrogen Storage/MWh
Late-winter high-volatility disturbance day	0	1904.46	14.96	3062.91	0.00
	250	1883.85	15.97	3055.30	0.01
	500	1863.95	16.86	3055.31	0.01
	1000	1818.80	19.41	3055.29	0.04
	2000	1730.79	24.32	3025.92	0.13
	3000	1650.74	27.98	3025.92	0.15
	5000	1620.40	29.69	2076.48	702.62
Summer surplus-hydrogen-storage day	0	1487.54	29.06	7068.01	1357.07
	250	1476.42	29.69	7060.41	1476.62
	500	1476.42	29.69	7060.41	1726.62
	1000	1476.42	29.69	7060.41	2226.62
	2000	1476.42	29.69	7060.41	3226.62
	3000	1476.42	29.69	7060.41	4226.62
	5000	1476.42	29.69	5140.99	4307.20
Transition-season thermal-power-support day	0	2314.54	2.08	399.65	0.00
	250	2292.67	3.31	391.34	0.00
	500	2270.05	4.58	391.25	0.00
	1000	2227.27	6.95	362.13	0.00
	2000	2155.92	11.25	356.63	0.03
	3000	2071.48	13.95	356.63	0.05
	5000	1898.60	23.35	356.63	0.01

Note: The initial hydrogen storage level represents the storage state at the beginning of each representative day.

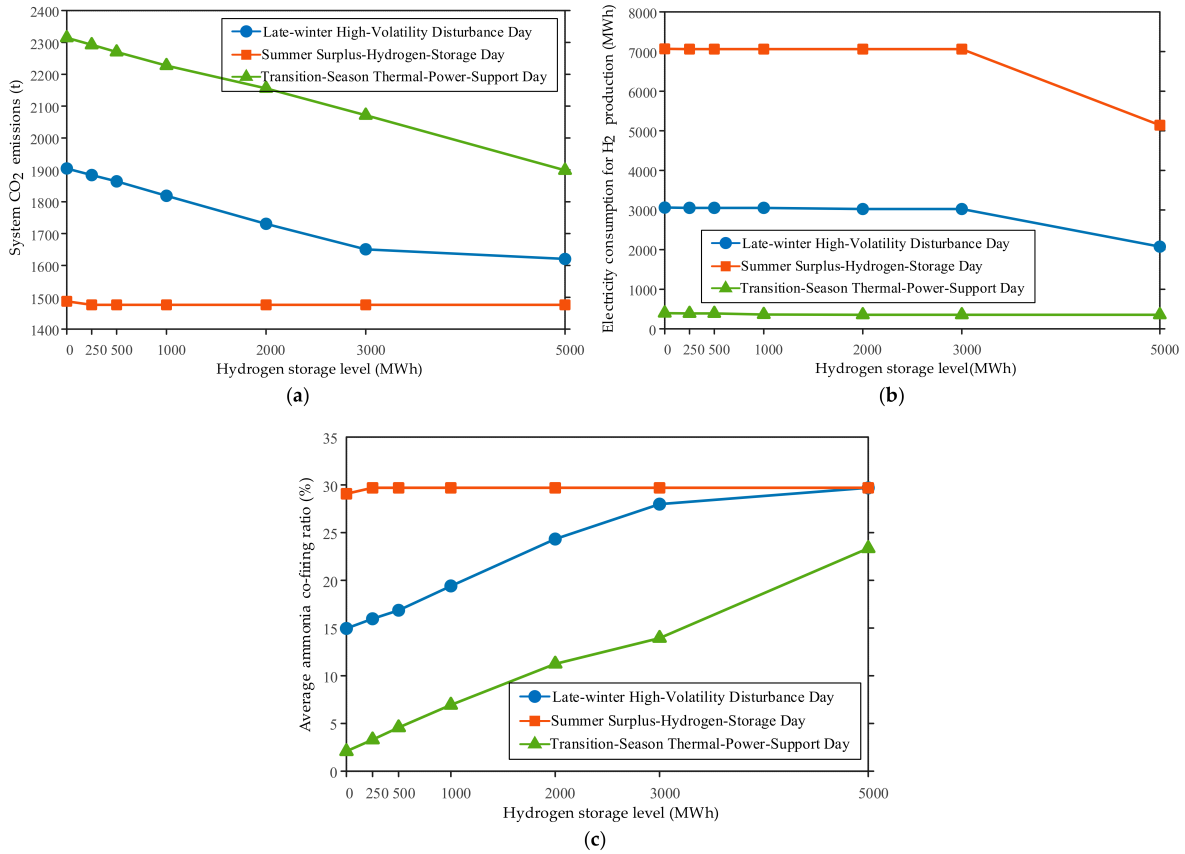


Figure 8. Effects of the initial hydrogen storage level on system operating performance: (**a**) system CO_2 emissions; (**b**) electricity consumption for hydrogen production; (**c**) average ammonia co-firing ratio.

4.2.2. Multi-Objective Weight Sensitivity Analysis

The weight sensitivity results are presented in Table 4. The system operation is sensitive to the variation of W_{CO_2}, particularly at relatively low weight values. When W_{CO_2} increases from 10^2 to 10^3, the system CO_2 emissions decrease from 2399.26 t to 2228.09 t, while grid electricity purchases decrease from 142.39 MWh to 45.65 MWh. Further increasing W_{CO_2} to 10^4 reduces these two indicators to 2227.27 t and 41.52 MWh, respectively. However, both indicators remain almost unchanged when W_{CO_2} increases from 10^4 to 10^8, indicating that excessive increases in the CO_2 emission weight have limited effects on the optimization results. In comparison, varying W_{buy} from 10^0 to 10^6 causes only minor changes in system CO_2 emissions and grid electricity purchases. Therefore, the scheduling results are relatively insensitive to W_{buy} under the considered operating condition.

Table 4. Results of the multi-objective weight sensitivity analysis.

Varied Weight	Weight Value	System CO_2 Emissions/t	Grid Electricity Purchase/MWh
W_{CO_2}	10^2	2399.26	142.39
	10^3	2228.09	45.65
	10^4	2227.27	41.52
	10^5	2227.27	41.52
	10^6–10^8	2227.27	41.52
W_{buy}	10^0–10^6	2227.27	41.52
W_{ramp}	10^{-1}–10^3	2227.27	41.52
	10^4	2233.97	75.00
	10^5	2352.55	574.99
	10^6	2373.14	716.04

The influence of W_{ramp} on system operation is more significant. When W_{ramp} varies from 10^{-1} to 10^3, the system CO_2 emissions and grid electricity purchases remain nearly unchanged, with values of approximately 2227.27 t and 41.52 MWh, respectively. However, increasing W_{ramp} to 10^4 leads to increases in both indicators, reaching 2233.97 t and 75.00 MWh. Further increases in W_{ramp} to 10^5 and 10^6 result in higher grid electricity purchases of 574.99 MWh and 716.04 MWh, respectively, accompanied by increases in system CO_2 emissions to 2352.55 t and 2373.14 t.

As shown in Figure 9, the thermal power output trajectories are similar under relatively low W_{ramp} values. With increasing W_{ramp} the output trajectories become smoother and the mean absolute ramping magnitude decreases. When W_{ramp} reaches 10^5 and 10^6, the mean absolute ramping magnitudes decrease to approximately 2.22 MWh and 0.31 MWh, respectively. This indicates that increasing the ramping weight can effectively suppress thermal power fluctuations between consecutive dispatch intervals. However, an excessively large W_{ramp} restricts the adjustment capability of thermal power units, resulting in increased grid electricity purchases and system CO_2 emissions.

Based on the sensitivity analysis results, $W_{CO_2} = 10^5$, $W_{buy} = 10^3$, and $W_{ramp} = 10^2$ are selected as the baseline weight combination for subsequent simulations. This combination prioritizes CO_2 emission reduction while maintaining sufficient thermal power adjustment capability to respond to system power imbalances.

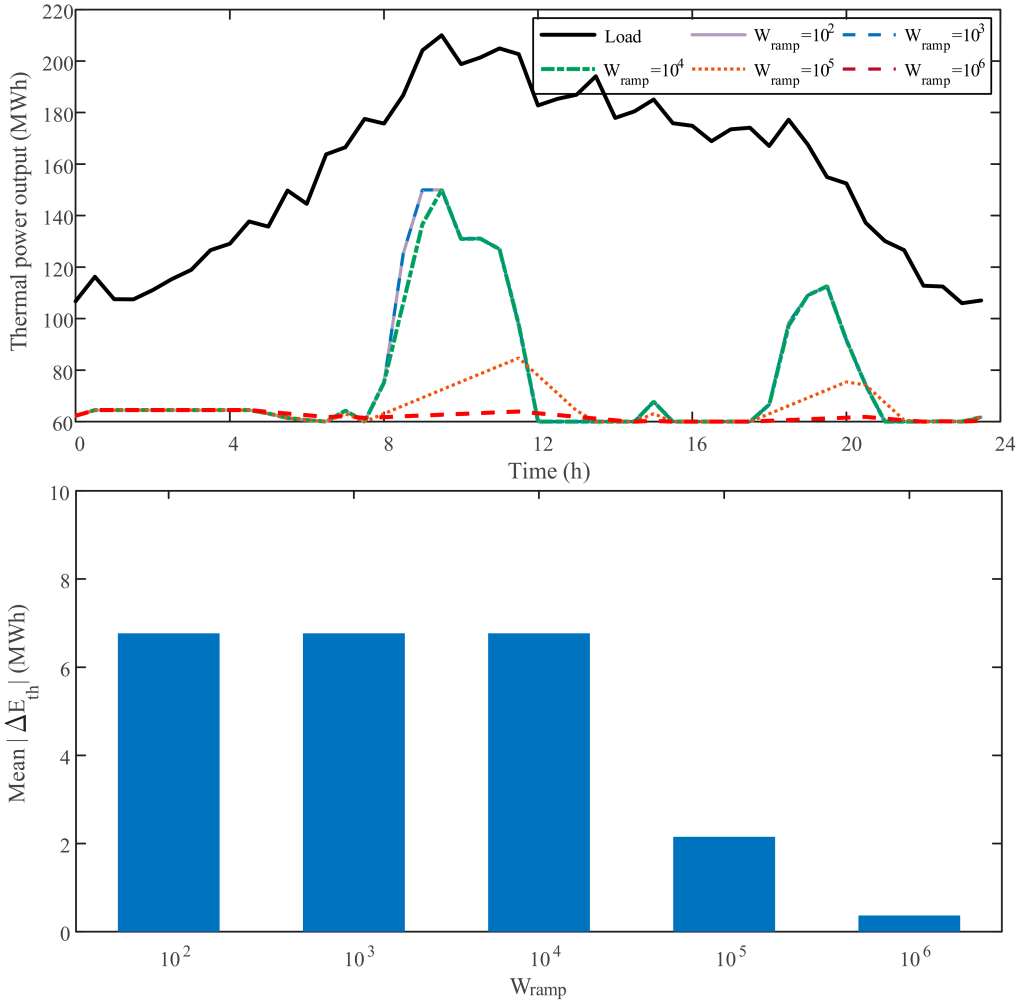


Figure 9. Thermal power output trajectories and ramping characteristics under different ramping weights.

4.2.3. Hydrogen Availability and Time-Step Sensitivity Analysis

To evaluate the temporal causality constraint on hydrogen utilization, the proposed model was compared with a model allowing current-interval hydrogen utilization under otherwise identical operating conditions. As shown in Table 5, the effects of the temporal causality constraint on system operational CO_2 emissions, end-of-day hydrogen storage levels, and average ammonia co-firing ratios were quantified and remained limited under the investigated scenarios. However, the alternative model relied on current-interval hydrogen production in five winter intervals and one transition-season interval, where hydrogen available from the previous interval was insufficient. This result demonstrates the role of the hydrogen availability constraint in maintaining temporal consistency of hydrogen utilization.

Time-step sensitivity was further examined using 0.5 h and 1 h dispatch intervals under equivalent operating conditions. The changes in system operational CO_2 emissions were −0.76%, −0.39%, and −0.34% for the winter, summer, and transition-season scenarios, respectively, with a maximum difference of 0.43 percentage points in the average ammonia co-firing ratio. The summer end-of-day hydrogen storage level changed from 2226.62 to 2144.55 MWh, indicating that hydrogen storage evolution exhibits some sensitivity to dispatch resolution. This difference mainly results from the different temporal aggregation of hydrogen production and utilization within each dispatch interval.

Table 5. Effects of Hydrogen Availability Constraint and Dispatch Time-Step on System Operation.

Typical Scenario	Dispatch Setting	System CO_2 Emissions/t	Average Ammonia Co-Firing Ratio/%	End-of-Day Hydrogen storage/MWh
Late-winter high-volatility disturbance day	0.5 h, Proposed	1818.80	19.41	0.04
	0.5 h, Same-interval	1818.88	19.40	0.03
	1 h, Proposed	1804.91	18.98	0.01
Summer surplus-hydrogen-storage day	0.5 h, Proposed	1476.42	29.69	2226.62
	0.5 h, Same-interval	1476.42	29.69	2226.62
	1 h, Proposed	1470.72	30.00	2144.55
Transition-season thermal-power-support day	0.5 h, Proposed	2227.27	6.95	0.00
	0.5 h, Same-interval	2227.19	6.94	0.05
	1 h, Proposed	2219.73	6.90	0.06

Note: Proposed denotes the model with the temporal causality constraint on hydrogen utilization; Same-interval allows hydrogen produced during the current dispatch interval to be used within that interval.

4.3. Comparison of Different EMS Optimization Methods

For the GA comparison, the same simulation conditions, objective function, and operating constraints as those of the proposed PSO-based EMS are adopted, while the optimal solution is obtained through the population evolution process of GA. The single-step baseline method adopts the same energy-flow model and operating constraints, including the temporal causality constraint on hydrogen utilization. Specifically, ammonia synthesis during the current dispatch interval can only use the hydrogen stored at the end of the previous interval, while hydrogen newly produced in the current interval is used to update the hydrogen storage state. Unlike PSO and GA, the single-step baseline method determines the operating point through a deterministic rule-based dispatch strategy without population-based optimization A comparison of the results from the three algorithms is presented in Table 6.

Table 6. Comparison of EMS performance using different optimization methods under three typical operating scenarios.

Typical Scenario	Optimization Method	System CO_2 Emissions/t	CO_2 Reduction Rate/%	Average Ammonia Co-Firing Ratio/%	Grid Electricity Purchase/MWh
Late-winter high-volatility disturbance day	PSO	1818.80	18.91	19.41	14.29
	GA	1826.16	18.87	19.36	14.34
	Single-step baseline	1949.32	11.54	13.03	50.43
Summer surplus-hydrogen-storage day	PSO	1476.42	29.70	29.69	0.00
	GA	1506.24	28.62	28.60	0.00
	Single-step baseline	1640.67	20.79	20.75	0.00
Transition-season thermal-power-support day	PSO	2227.27	5.06	6.95	41.52
	GA	2229.53	5.06	6.94	41.50
	Single-step baseline	2269.42	2.75	4.63	68.31

Note: The pure-coal baseline CO_2 emissions and the corresponding emission reduction rates are calculated separately for each method based on its own thermal power output trajectory.

The results show that PSO and GA achieve similar operating results for the late-winter high-volatility disturbance day and the transition-season thermal-power-support day, and both methods outperform the single-step baseline method under these scenarios. The largest difference is observed for the summer surplus-hydrogen-storage day. PSO achieves an average ammonia co-firing ratio of 29.69% and a CO_2 emission reduction rate of 29.70%, compared with 28.60% and 28.62% for GA, and 20.75% and 20.79% for the single-step baseline method, respectively.

For the summer surplus-hydrogen-storage day, the single-step baseline method results in a lower average ammonia co-firing ratio and higher CO_2 emissions than PSO and GA. Although all three methods satisfy the same temporal hydrogen-availability constraint,

their decision-making strategies differ. The single-step baseline method determines the operating point through predefined dispatch rules, whereas PSO jointly optimizes thermal power output and the ammonia co-firing ratio according to the multi-objective fitness function. Under the considered operating conditions, PSO achieves better coordination between these two decision variables, resulting in a higher ammonia co-firing ratio and lower system CO_2 emissions.

Overall, under the interval-by-interval EMS framework and the considered simulation conditions, PSO achieves comparable or better CO_2 emission performance than GA across the three representative scenarios. Compared with the single-step baseline method, PSO provides improved coordination between thermal power output and ammonia co-firing ratio. However, since the differences between PSO and GA are relatively small in some scenarios, these results do not indicate the universal superiority of PSO over GA.

4.4. Year-Round Continuous Simulation Results

Based on the settings described in Section 3.2, a 365-day continuous simulation is conducted to evaluate the long-term operating characteristics of the proposed EMS.

As shown in Figure 10, the ammonia co-firing ratio varies dynamically between 0 and 0.30 throughout the year in response to hydrogen availability and system operating conditions. During periods with sufficient surplus wind energy, the remaining wind energy is used for electrolytic hydrogen production, replenishing the hydrogen storage level and providing hydrogen for subsequent coal–ammonia co-firing. As hydrogen availability decreases, the ammonia co-firing ratio is reduced accordingly. When the hydrogen stored at the end of the previous dispatch interval is insufficient to support the required ammonia co-firing ratio, the EMS further reduces the co-firing ratio and, when necessary, switches the unit to pure-coal operation. This operating behavior is consistent with the storage-before-utilization mechanism and the temporal causality constraint on hydrogen utilization established in this study.

The hydrogen storage level remains within the allowable range of 0–5000 MWh throughout the year. The maximum hydrogen storage level reaches 5000 MWh, while the end-of-year level is 75.05 MWh. The annual average ammonia co-firing ratio is 7.21%. Dispatch intervals at the upper limit of 0.30 account for 19.32% of the year, whereas pure-coal operating intervals account for 69.54%. These results indicate that high ammonia co-firing ratios occur mainly during periods with favorable wind energy and hydrogen storage conditions, while limited hydrogen availability leads to lower ammonia co-firing ratios or pure-coal operation during a substantial portion of the year.

As shown in Table 7, the year-round system operational CO_2 emissions are 961.255 kt, representing a reduction of 37.713 kt relative to the pure-coal baseline of 998.968 kt under the same thermal power output trajectory. The corresponding annual system CO_2 emission reduction rate is 3.78%. Annual grid electricity purchases amount to 30,765 MWh, while electricity sales to the grid reach 374,201 MWh. No wind energy curtailment occurs during the year-round simulation under the considered grid exchange capacity and operating conditions. This result indicates that the available wind energy is accommodated either through internal electricity consumption or grid export rather than curtailment. Although the hydrogen storage level decreases from 1000 to 75.05 MWh during the annual simulation, a conservative upper-bound estimate indicates that the corresponding net storage depletion accounts for only approximately 0.26% of the total annual CO_2 reduction. Therefore, the influence of the initial hydrogen storage level on the reported annual CO_2 emission reduction result is limited.

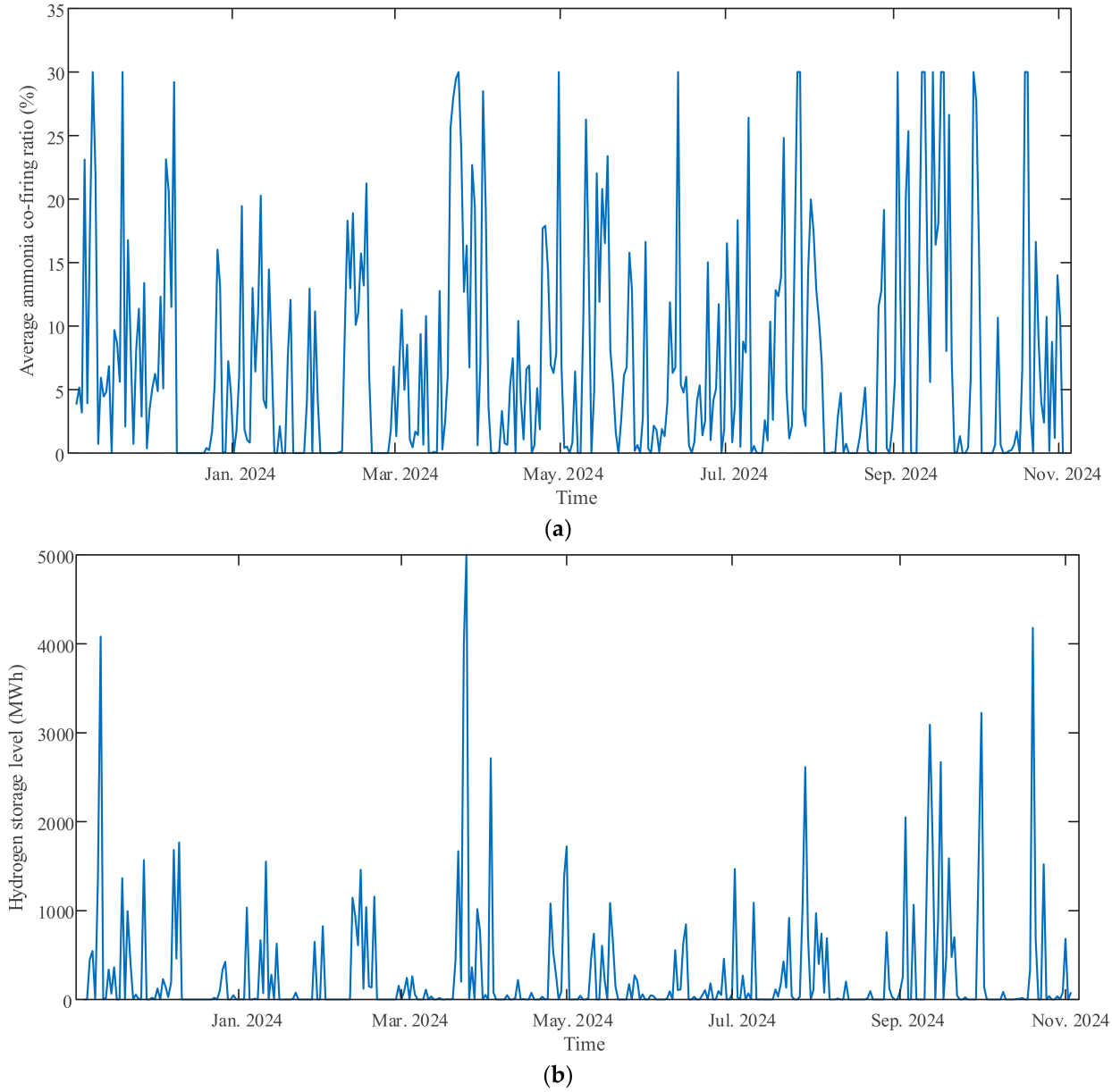


Figure 10. Year-round variations in the ammonia co-firing ratio and hydrogen storage trajectory. (**a**) Annual Daily Average Ammonia Co-firing Ratio; (**b**) Hydrogen Storage Level at the End of Each Day.

The relatively large annual electricity sales are associated with both surplus wind energy and the operating constraints of the system. During periods with abundant wind energy, surplus electricity is exported to the grid after the electricity demands for ammonia synthesis, load supply, and electrolytic hydrogen production are satisfied. In some dispatch intervals, the minimum allowable thermal power output and ramping constraints limit further or rapid reductions in thermal power output, thereby increasing the electricity available for grid export. The relatively large annual electricity sales therefore result from the combined effects of surplus wind energy, the internal electricity consumption capability of the system, and constraints on thermal power output adjustment.

The year-round results, together with the typical-day analysis, show that the nearly 30% daily CO_2 emission reduction observed on the surplus-hydrogen-storage day represents the operating potential under favorable wind energy and hydrogen storage conditions rather than the annual average emission reduction performance. During continuous opera-

tion, system low-carbon performance depends on the temporal distribution of wind energy, hydrogen availability, and the requirement for thermal power support. Evaluation of the Wind–Hydrogen–Ammonia Coupled Thermal Power System should therefore consider both representative short-term operating scenarios and year-round continuous operation.

Table 7. Main Operating Indicators of Year-Round Continuous Operation.

Indicator	Unit	Year-Round Result
Initial hydrogen storage level	MWh	1000
End-of-year hydrogen storage level	MWh	75.05
Maximum annual hydrogen storage level	MWh	5000
Pure-coal baseline CO_2 emissions under the same thermal power output trajectory	kt	998.968
System CO_2 emissions	kt	961.255
Annual CO_2 emission reduction	kt	37.713
Annual system CO_2 emission reduction rate	%	3.78
Annual average ammonia co-firing ratio	%	7.21
Proportion of dispatch intervals at $\alpha = 0.30$	%	19.32
Proportion of dispatch intervals under pure-coal operation	%	69.54
Annual grid electricity purchases	MWh	30,765
Annual electricity sales to the grid	MWh	374,201
Annual wind energy curtailment	MWh	0

Note: Hydrogen storage-related quantities are expressed in energy-based units (MWh). Zero wind energy curtailment does not indicate complete local consumption of wind energy, as surplus wind power can be exported to the grid.

5. Conclusions

This study investigates the low-carbon operation of a Wind–Hydrogen–Ammonia Coupled Thermal Power System. A multi-energy-flow coupling model and an interval-by-interval EMS considering the temporal causality of hydrogen utilization are developed with a 0.5 h dispatch resolution. PSO is employed to coordinate thermal power output and the ammonia co-firing ratio during each dispatch interval. The proposed strategy is evaluated through nine typical-day simulations, parameter sensitivity analyses, algorithm comparisons, and a year-round continuous simulation. The main conclusions are summarized as follows.

(1) The proposed EMS represents the temporal causality of hydrogen utilization by distinguishing hydrogen stored at the end of the previous dispatch interval from hydrogen newly produced during the current interval. Therefore, the ammonia co-firing ratio in the current interval is constrained by the hydrogen availability inherited from the previous interval. Combined with the dynamic operating constraints of thermal power units and the hydrogen-availability-based emergency reduction mechanism, this strategy maintains temporal consistency and ensures operational feasibility at the dispatch level.

(2) The CO_2 emission reduction performance under different operating scenarios is jointly affected by thermal power output and hydrogen availability. The average ammonia co-firing ratios for the late-winter high-volatility disturbance day, summer surplus-hydrogen-storage day, and transition-season thermal-power-support day are 19.41%, 29.69%, and 6.95%, respectively, corresponding to CO_2 emission reduction rates of 18.91%, 29.70%, and 5.06%. The results from the nine typical-day scenarios indicate that higher surplus wind energy availability provides more favorable conditions for

electrolytic hydrogen production and storage, thereby supporting higher ammonia co-firing ratios and reducing coal consumption.

(3) The sensitivity analysis shows that an excessively low initial hydrogen storage level limits the achievable ammonia co-firing ratio, whereas an excessively high initial hydrogen storage level reduces the available storage capacity for subsequent hydrogen production. Considering the results under the three representative scenarios, an initial hydrogen storage level of 1000 MWh is selected as the baseline setting. The weight sensitivity analysis further indicates that an excessively low W_{CO_2} reduces the relative emphasis on the CO_2 emission objective, whereas an excessively high W_{ramp} imposes excessive restrictions on thermal power output adjustment. Accordingly, $W_{CO_2} = 10^5$, $W_{buy} = 10^3$, and $W_{ramp} = 10^2$ are selected as the baseline weight combination.

(4) Under the three representative scenarios, PSO achieves comparable or better CO_2 emission performance than GA and provides better coordination between thermal power output and the ammonia co-firing ratio than the single-step baseline method. In the year-round continuous simulation, system operational CO_2 emissions decrease from 998.968 kt for the pure-coal baseline under the same thermal power output trajectory to 961.255 kt, corresponding to an annual CO_2 emission reduction rate of 3.78%. The annual average ammonia co-firing ratio is 7.21%. These results indicate that the high emission reduction potential observed under favorable surplus-wind conditions does not represent the annual average performance of the system. During continuous operation, CO_2 emission reduction remains dependent on the temporal distribution of wind energy, hydrogen availability, and thermal power support requirements.

Finally, the limitations of this study should be noted. The proposed model is developed at the dispatch level with a 0.5 h resolution and focuses on operational CO_2 emissions. The detailed electrical and mechanical conversion processes of individual components, including wind turbines, electrolyzers, hydrogen storage systems, ammonia synthesis units, and thermal power units, are not explicitly modeled. In addition, NO_x, N_2O, ammonia slip, hydrogen storage losses, and variations in boiler efficiency and combustion stability caused by ammonia co-firing are not considered. The fast dynamic responses of the boiler and fuel, air, and ammonia supply systems are also beyond the scope of the current model.

Furthermore, the comparative evaluation of EMS optimization methods is currently limited to GA and the single-step baseline method. Future work will incorporate more detailed equipment characteristics and combustion mechanisms and further evaluate the proposed EMS using additional advanced optimization approaches.

Author Contributions: Methodology, G.W.; software, G.W., K.Q. (assistance with parameter setting and debugging of the particle swarm optimization (PSO) algorithm), S.L. (assistance with the development and improvement of the ammonia co-firing system model), and X.L. (assistance with debugging the data input model); validation, G.W.; writing—original draft preparation, G.W.; writing—review and editing, G.W. and J.W.; funding acquisition, J.W. All authors have read and agreed to the published version of the manuscript.

Funding: This paper is supported by Inner Mongolia Natural Science Foundation Project under grant No: 2025LHMS05018 and Inner Mongolia First-Class Discipline scientific research special project under grant No: YLXKZX-NGD-011.

Data Availability Statement: The data presented in this study are not publicly available but can be obtained from the corresponding author upon reasonable request.

Acknowledgments: The authors sincerely thank the three anonymous reviewers for their careful evaluation and constructive comments, which have helped improve this study and will guide future refinement of the proposed EMS and comparisons with other representative optimization algorithms.

Conflicts of Interest: Author Kai Qi was employed by the company Inner Mongolia Three Gorges Mengneng Energy Co., Ltd. Author Suyao Liu was employed by the company China Resources New Energy Investment Co., Ltd., Inner Mongolia Branch. The remaining authors declare that the research was conducted in the absence of any commercial or financial relationships that could be construed as a potential conflict of interest. The authors declare that this study received funding from the Inner Mongolia Natural Science Foundation Project (Grant No. 2025LHMS05018) and the Inner Mongolia First-Class Discipline Scientific Research Special Project (Grant No. YLXKZX-NGD-011). The funders were not involved in the study design, collection, analysis, interpretation of data, the writing of this article, or the decision to submit it for publication.

Abbreviations

Abbreviation/Symbol	Unit	Description
EMS	-	Energy Management System
PSO	-	Particle Swarm Optimization
t	-	Dispatch interval index
$E_{\mathrm{wind}}(t)$	MWh	Wind energy input during dispatch interval t
$E_{\mathrm{load}}(t)$	MWh	Load demand during dispatch interval t
$E_{\mathrm{th}}(t)$	MWh	Thermal power output during dispatch interval t
$E_{\mathrm{grid}}(t)$	MWh	Electricity exchanged with the grid during dispatch interval t
$E_{\mathrm{wind,H_2}}(t)$	MWh	Wind energy allocated to hydrogen production by electrolysis during dispatch interval t
$E_{\mathrm{wind,NH_3}}(t)$	MWh	Wind energy allocated to ammonia synthesis during dispatch interval t
$H(t)$	MWh	Hydrogen storage level at the end of dispatch interval t
$H_{\mathrm{dem}}(t)$	MWh	Hydrogen consumption for ammonia synthesis during dispatch interval t
$H_{\mathrm{prod}}(t)$	MWh	Hydrogen production from electrolysis during dispatch interval t
$M_{\mathrm{coal,base}}(t)$	t	Baseline coal consumption under pure-coal operation during interval t
$M_{\mathrm{coal,act}}(t)$	t	Actual coal consumption under coal–ammonia co-firing during interval t
$M_{\mathrm{NH_3}}(t)$	t	Ammonia consumption during interval t
$\mathrm{CO_{2,system}}(t)$	t	Operational CO_2 emissions of the system during interval t
$\alpha(t)$	-	Ammonia co-firing ratio during dispatch interval t

References

1. Pilpola, S.; Arabzadeh, V.; Lund, P.D. Energy system impact of wind power with curtailment: National- and city-scale analysis. *Int. J. Low. Carbon Technol.* **2019**, *14*, 277–285. [CrossRef]
2. Suri, D.; de Chalendar, J.; Azevedo, I.M.L. Assessing the real implications for CO_2 as generation from renewables increases. *Nat. Commun.* **2025**, *16*, 7124. [CrossRef] [PubMed]
3. Kiviluoma, J.; O'Dwyer, C.; Ikäheimo, J.; Lahon, R.; Li, R.; Kirchem, D.; Helistö, N.; Rinne, E.; Flynn, D. Multi-sectoral flexibility measures to facilitate wind and solar power integration. *IET Renew. Power Gener.* **2022**, *16*, 1814–1826. [CrossRef]
4. Parisio, A. Towards network-aware operation of integrated energy systems: A comprehensive review. *arXiv* **2026**, arXiv:2603.07266.
5. Cao, Y.; Xu, Y. Secure operation of a multi-energy system: A comprehensive review. *Renew. Sustain. Energy Rev.* **2025**, *211*, 115312. [CrossRef]
6. Zubo, R.H.A.; Onen, P.S.; Mujtaba, I.M.; Mokryani, G.; Abd-Alhameed, R. Optimal scheduling of a multi-energy hub with integrated demand response programs. *Processes* **2025**, *13*, 2879. [CrossRef]
7. Chen, B.; Guo, Q.; Yin, G.; Wang, B.; Pan, Z.; Chen, Y.; Wu, W.; Sun, H. Energy-circuit-based integrated energy management system: Theory, implementation, and application. *Proc. IEEE* **2022**, *110*, 1897–1926. [CrossRef]
8. Chen, B.; Liao, Q.; Liu, D.; Wang, W.; Wang, Z.; Chen, S. Comprehensive evaluation indices and methods for regional integrated energy system. *Autom. Electr. Power Syst.* **2018**, *42*, 174–182. (In Chinese)
9. Chen, Y.; Sun, H.; Guo, Q. Energy circuit theory of integrated energy system analysis (V): Integrated electricity–heat–gas dispatch. *Proc. CSEE* **2020**, *40*, 7928–7937. (In Chinese)
10. Yin, S.; Ai, Q.; Jiang, Z.; Sun, D.; Li, X. Collaborative optimal strategy of real-time market bidding and energy management for integrated energy station on the demand side. *Proc. CSEE* **2021**, *41*, 4490–4501. (In Chinese)

11. Xiao, B.; Liu, Y.; Ye, Y.; Liu, W.; Zhong, Z.; Fang, J.; Huang, L.; Wang, H. Real-time energy management strategy of photovoltaic–energy storage–hydrogen production integrated system considering generalized energy storage participating in flexible response. *Electr. Power Autom. Equip.* **2024**, *44*, 53–61. (In Chinese)
12. Ishaq, H.; Crawford, C. Review of ammonia production and utilization: Enabling clean energy transition and net-zero climate targets. *Energy Convers. Manag.* **2024**, *300*, 117869. [CrossRef]
13. Kumar, L.; Sleiti, A.K. Systematic review on ammonia as a sustainable fuel for combustion. *Renew. Sustain. Energy Rev.* **2024**, *202*, 114699. [CrossRef]
14. Mayer, P.; Ramirez, A.; Pezzella, G.; Winter, B.; Sarathy, S.M.; Gascon, J.; Bardow, A. Blue and green ammonia production: A techno-economic and life cycle assessment perspective. *iScience* **2023**, *26*, 107389. [CrossRef] [PubMed]
15. Sun, Y.; Li, Z.; Wang, Q.; Zhang, J.; Kong, H. Low carbon pathway and life cycle assessment of ammonia co-firing in coal power plants under the context of carbon neutrality. *Energy Convers. Manag.* **2023**, *296*, 117648. [CrossRef]
16. JERA Co., Inc. Conclusion of Fuel Ammonia Substitution Demonstration Testing at Hekinan Thermal Power Station. 26 June 2024. Available online: https://www.jera.co.jp/en/news/notice/20240626_1954 (accessed on 10 September 2026).
17. Lin, Q.; Sun, W.; Li, H.; Liu, Y.; Chen, Y.; Liu, C.; Jiang, Y.; Cheng, Y.; Ma, N.; Ya, H.; et al. Experimental study on ammonia co-firing with coal for carbon reduction in the boiler of a 300-MW coal-fired power station. *Engineering* **2024**, *40*, 247–259. [CrossRef]
18. Yuan, W.; Chen, L.; Wang, C.; Wang, Z. Bi-level optimal scheduling of power-to-ammonia coupling wind–photovoltaic–thermal integrated energy system based on ammonia energy storage technology. *Proc. CSEE* **2023**, *43*, 6992–7002. (In Chinese)
19. Liang, J.; Zhang, G.; Li, F.; Xie, C.; Wang, T. Low-carbon optimal scheduling of integrated energy system considering hydrogen energy storage, ammonia production and carbon capture. *Electr. Power Autom. Equip.* **2024**, *44*, 16–23. (In Chinese)
20. Xu, J.; Zhu, H.; Xu, Y.; Yu, D. Research progress and prospect of ammonia cofiring in utility coal-fired boiler. *J. Huazhong Univ. Sci. Technol. Nat. Sci. Ed.* **2022**, *50*, 55–65. (In Chinese)
21. Yu, Z.; Lin, J.; Lei, J.; Wang, Y.; Song, Y.; Jiang, L.; Pan, J.; Zhang, X. Multi-stage decarbonization planning for receiving-end power systems considering thermal power generation with hydrogen-ammonia cofiring. *Autom. Electr. Power Syst.* **2025**, *49*, 57–68. (In Chinese)
22. Zhang, W.; Liu, J. Low-carbon optimal dispatch of park integrated energy system considering coordinated ammonia production from multiple hydrogen energy. *Renew. Energy* **2024**, *237*, 121712. [CrossRef]
23. Zhou, B.X.; Zhu, W.C.; Zhu, J.; Qiu, Y.W.; Zang, T.L.; He, G.; Chen, G. Multi-stage dispatchable region analysis of wind- and solar-power-based hydrogen production and ammonia synthesis system. *Proc. CSEE* **2024**, *44*, 160–173. (In Chinese)
24. Wu, T.; Jiang, Y.; Cui, S.; Li, Z.; Wang, S.; Zhai, J. Physically-bounded distributionally robust chance-constrained dispatch approach for power system with renewable power-to-ammonia. *Appl. Energy* **2026**, *402*, 126972. [CrossRef]
25. Cheng, L.; Ji, X. Optimal scheduling of weak-grid green ammonia systems based on ALK–PEM electrolyzer coordination. *Energies* **2026**, *19*, 2807. [CrossRef]
26. La Corte, D.; Maddaloni, M.; Vahidzadeh, R.; Domini, M.; Bertanza, G.; Ansari, S.U.; Marchionni, M.; Tola, V.; Artioli, N. Recovered ammonia as a sustainable energy carrier: Innovations in recovery, combustion, and fuel cells. *Energies* **2025**, *18*, 508. [CrossRef]
27. Xu, Y.; Wang, H.; Liu, X.; Zhu, J.; Xu, J.; Xu, M. Mitigating CO2 emission in pulverized coal-fired power plant via co-firing ammonia: A simulation study of flue gas streams and exergy efficiency. *Energy Convers. Manag.* **2022**, *256*, 115328. [CrossRef]
28. Lü, K.; Wang, H.Y.; Zhou, J.; Wang, D.Y.; Yang, R.Z. Study on the characteristics of electrothermal coal in cogeneration unit. *Therm. Power Gener.* **2018**, *47*, 42–48. (In Chinese)
29. Ding, X.; Li, W.; Ma, D. Discussion on coal-fired units coupled with ammonia fuel: Combustion characteristics and economy. *Therm. Power Gener.* **2022**, *51*, 20–28. (In Chinese)
30. *ISO 14044:2006*; Environmental Management—Life Cycle Assessment—Requirements and Guidelines. International Organization for Standardization: Geneva, Switzerland, 2006.
31. Alnajideen, M.; Shi, H.; Northrop, W.; Emberson, D.; Kane, S.; Czyzewski, P.; Alnaeli, M.; Mashruk, S.; Rouwenhorst, K.; Yu, C.; et al. Ammonia combustion and emissions in practical applications: A review. *Carbon Neutrality* **2024**, *3*, 13. [CrossRef]
32. Wang, G.; Zhao, J.; Zhang, H.; Wang, X.; Qin, H.; Wu, K.; Zhao, C.; Fan, W.; Xu, J. Ammonia co-firing with coal: A review of the status and prospects. *Energy Fuels* **2024**, *38*, 15861–15886. [CrossRef]
33. Wang, Y.; Yi, J.; Xie, X. Review of wind–solar–hydrogen–ammonia–methanol integrated technologies and industry. *Power Gener. Technol.* **2025**, *46*, 556–569. (In Chinese)
34. Narciso, D.A.C.; Pires, J.M.; Fortunato, J.; Teixeira, P.; Castro, P.M.; Pinheiro, C.I.C.; Matos, H.A. Design and operation of power-to-ammonia systems: A review. *Energy Convers. Manag.* **2025**, *327*, 119494. [CrossRef]
35. Zhao, F.; Li, Y.; Zhou, X.; Wang, D.; Wei, Y.; Li, F. Co-optimization of decarbonized operation of coal-fired power plants and seasonal storage based on green ammonia co-firing. *Appl. Energy* **2023**, *341*, 121140. [CrossRef]
36. Corigliano, O.; Genovese, M.; Fragiacomo, P. Dynamic modeling and simulation of a hydrogen power station for continuous energy generation and resilient storage. *J. Power Sources* **2025**, *629*, 236076. [CrossRef]

37. Ahmed, N.; Gerdun, P.; Weber, H. Active power control based on hydrogen availability in a storage power plant. *IFAC Pap.* **2020**, *53*, 12708–12713. [CrossRef]
38. Sun, Z.; Zhang, Y.; Huang, H.; Luo, Y.; Lin, L.; Jiang, L. Modeling and simulation of dynamic characteristics of a green ammonia synthesis system. *Energy Convers. Manag.* **2024**, *300*, 117893. [CrossRef]
39. Kobayashi, H.; Hayakawa, A.; Somarathne, K.D.K.A.; Okafor, E.C. Science and technology of ammonia combustion. *Proc. Combust. Inst.* **2019**, *37*, 109–133. [CrossRef]
40. Jin, W.; Si, F.; Cao, Y.; Yu, C.; Wang, J. Numerical research on ammonia-coal co-firing in a 1050 MW coal-fired utility boiler under ultra-low load: Effects of ammonia ratio and air staging condition. *Appl. Therm. Eng.* **2023**, *233*, 121100. [CrossRef]
41. Ghasaei, A. Hierarchical Discrete-Event Supervisory Control of AC Multi-Microgrid Systems. Ph.D. Thesis, University of Toronto, Toronto, ON, Canada, 2021.
42. Alshammari, N.F.; Alyami, F.H.; Iqbal, S.; Shafiullah, M.; Al Dawsari, S. Adaptive preference-based multi-objective energy management in smart microgrids: A novel hierarchical optimization framework with dynamic weight allocation and advanced constraint handling. *Sustainability* **2026**, *18*, 3591. [CrossRef]
43. Khare, A.; Rangnekar, S. A review of particle swarm optimization and its applications in solar photovoltaic system. *Appl. Soft Comput.* **2013**, *13*, 2997–3006. [CrossRef]
44. Sharma, R.; Matharu, J.S.; Parmar, K.S. A survey on particle swarm optimization: Evolution, adaptations and practical implementations. *Appl. Soft Comput.* **2026**, *186*, 114016. [CrossRef]
45. Ministry of Ecology and Environment of the People's Republic of China; National Bureau of Statistics of China. Announcement on the Release of the 2023 Electricity CO_2 Emission Factors, Announcement No. 47 of 2025. 2025. Available online: https://www.mee.gov.cn/xxgk2018/xxgk/xxgk01/202512/t20251231_1139517.html (accessed on 30 September 2026).
46. Qu, Z.X. Discussion and calculation analysis of carbon emission allocation method for cogeneration units. *Shanghai Energy Sav.* **2025**, *12*, 1913–1916. (In Chinese)
47. Li, M.; Shi, A.; Shi, Y.; Zhang, T.; Qu, C.; Ye, L. Hybrid improved PSO algorithm for soil property parameter estimation. *Appl. Sci.* **2025**, *15*, 4451. [CrossRef]

Disclaimer/Publisher's Note: The statements, opinions and data contained in all publications are solely those of the individual author(s) and contributor(s) and not of MDPI and/or the editor(s). MDPI and/or the editor(s) disclaim responsibility for any injury to people or property resulting from any ideas, methods, instructions or products referred to in the content.